

2

AFOSR-TR- 01 0549

AFOSR Final Technical Report
for Grant Number
AFOSR-88-0014

DTIC
8
C

AD-A237 859



"Picosecond Studies of Chemical Intermediates"

November 1988 - March 1991

P.I. K. B. Eisenthal

Department of Chemistry

Columbia University New York, New York 10027

May 1991

Prepared for the Air Force Office of Scientific Research

91-04520



91 7 09 093

Approved for public release;
distribution unlimited.

REPORT DOCUMENTATION PAGE			Form Approved OASD No. 0704-0188	
<small>Public reporting burden for this collection of information is estimated to average 1 hour per response, including the time for reviewing instructions, searching existing data sources, gathering and maintaining the data needed, and completing and reviewing the collection of information. Send comments regarding this burden estimate or any other aspect of this collection of information, including suggestions for reducing this burden, to Washington Headquarters Services, Directorate for Information Operations and Reports, 1215 Jefferson Davis Highway, Suite 1204, Arlington, VA 22202-4302, and to the Office of Management and Budget, Paperwork Reduction Project (0704-0188), Washington, DC 20503.</small>				
1. AGENCY USE ONLY (Leave blank)		2. REPORT DATE May 1991		3. REPORT TYPE AND DATES COVERED Final Technical Report 11/88-3/91
4. TITLE AND SUBTITLE Picosecond Studies of Chemical Intermediates			5. FUNDING NUMBERS	
6. AUTHOR(S) K.B. Eisenthal				
7. PERFORMING ORGANIZATION NAME(S) AND ADDRESS(ES) Columbia University Box 20, Low Memorial Library New York, New York 10027			8. PERFORMING ORGANIZATION REPORT NUMBER	
9. SPONSORING / MONITORING AGENCY NAME(S) AND ADDRESS(ES) AFOSR/NC Building 410, Bolling AFB DC 20332-6448			10. SPONSORING / MONITORING AGENCY REPORT NUMBER AFOSR-88-0014	
11. SUPPLEMENTARY NOTES				
12a. DISTRIBUTION / AVAILABILITY STATEMENT Approved for public release; distribution is unlimited			12b. DISTRIBUTION CODE	
13. ABSTRACT (Maximum 200 words) <p>Surface second harmonic generation (SSHG) has been used to study the chemical and physical properties of liquid interfaces. Information about the thermodynamics of neat liquid surfaces has been found by observing the SH signal as a function of temperature. Extensive studies using monolayers at the air/water interface have been undertaken. Studies of acid/base equilibrium and monolayer phase transitions have been performed. The gas-liquid coexistence region and an orientational phase transition has been observed. SHG was used to study the interface properties of fused silica/electrolyte solution. Orientational relaxation has been observed on the picosecond time scale at the air/water interface by time-resolved second harmonic generation. The data suggests that the ground and excited states of Rhodamine 6G have different equilibrium orientational distributions.</p> <p>Femtosecond studies of electrons in liquids have characterized the geminate recombination and solvation dynamics of electrons in polar and nonpolar liquids. Photodetachment of electrons from halide ions in aqueous solution has also been studied. Picosecond studies of chemical intermediates have examined the role of</p>				
14. SUBJECT TERMS restricted geometries on elementary chemical processes.			15. NUMBER OF PAGES 53	
			16. PRICE CODE	
17. SECURITY CLASSIFICATION OF REPORT unclassified	18. SECURITY CLASSIFICATION OF THIS PAGE unclassified	19. SECURITY CLASSIFICATION OF ABSTRACT unclassified	20. LIMITATION OF ABSTRACT	

Surface second harmonic generation (SSHG) has been used to study the chemical and physical properties of liquid interfaces. Information about the thermodynamics of neat liquid surfaces has been found by observing the SH signal as a function of temperature. Extensive studies using monolayers at the air/water interface have been undertaken. Studies of acid/base equilibrium and monolayer phase transitions have been performed. The gas-liquid coexistence region and an orientational phase transition has been observed. SHG was used to study the interface properties of fused silica/electrolyte solution. Orientational relaxation has been observed on the picosecond time scale at the air/water interface by time-resolved second harmonic generation. The data suggests that the ground and excited states of Rhodamine 6G have different equilibrium orientational distributions.

Femtosecond studies of electrons in liquids have characterized the geminate recombination and solvation dynamics of electrons in polar and non-polar liquids. Photodetachment of electrons from halide ions in aqueous solution has also been studied. Picosecond studies of chemical intermediates have examined the role of restricted geometries on elementary chemical processes.

1
 2
 3
 4
 5
 6
 7
 8
 9
 10
 11
 12
 13
 14
 15
 16
 17
 18
 19
 20
 21
 22
 23
 24
 25
 26
 27
 28
 29
 30
 31
 32
 33
 34
 35
 36
 37
 38
 39
 40
 41
 42
 43
 44
 45
 46
 47
 48
 49
 50
 51
 52
 53
 54
 55
 56
 57
 58
 59
 60
 61
 62
 63
 64
 65
 66
 67
 68
 69
 70
 71
 72
 73
 74
 75
 76
 77
 78
 79
 80
 81
 82
 83
 84
 85
 86
 87
 88
 89
 90
 91
 92
 93
 94
 95
 96
 97
 98
 99
 100
 101
 102
 103
 104
 105
 106
 107
 108
 109
 110
 111
 112
 113
 114
 115
 116
 117
 118
 119
 120
 121
 122
 123
 124
 125
 126
 127
 128
 129
 130
 131
 132
 133
 134
 135
 136
 137
 138
 139
 140
 141
 142
 143
 144
 145
 146
 147
 148
 149
 150
 151
 152
 153
 154
 155
 156
 157
 158
 159
 160
 161
 162
 163
 164
 165
 166
 167
 168
 169
 170
 171
 172
 173
 174
 175
 176
 177
 178
 179
 180
 181
 182
 183
 184
 185
 186
 187
 188
 189
 190
 191
 192
 193
 194
 195
 196
 197
 198
 199
 200
 201
 202
 203
 204
 205
 206
 207
 208
 209
 210
 211
 212
 213
 214
 215
 216
 217
 218
 219
 220
 221
 222
 223
 224
 225
 226
 227
 228
 229
 230
 231
 232
 233
 234
 235
 236
 237
 238
 239
 240
 241
 242
 243
 244
 245
 246
 247
 248
 249
 250
 251
 252
 253
 254
 255
 256
 257
 258
 259
 260
 261
 262
 263
 264
 265
 266
 267
 268
 269
 270
 271
 272
 273
 274
 275
 276
 277
 278
 279
 280
 281
 282
 283
 284
 285
 286
 287
 288
 289
 290
 291
 292
 293
 294
 295
 296
 297
 298
 299
 300
 301
 302
 303
 304
 305
 306
 307
 308
 309
 310
 311
 312
 313
 314
 315
 316
 317
 318
 319
 320
 321
 322
 323
 324
 325
 326
 327
 328
 329
 330
 331
 332
 333
 334
 335
 336
 337
 338
 339
 340
 341
 342
 343
 344
 345
 346
 347
 348
 349
 350
 351
 352
 353
 354
 355
 356
 357
 358
 359
 360
 361
 362
 363
 364
 365
 366
 367
 368
 369
 370
 371
 372
 373
 374
 375
 376
 377
 378
 379
 380
 381
 382
 383
 384
 385
 386
 387
 388
 389
 390
 391
 392
 393
 394
 395
 396
 397
 398
 399
 400
 401
 402
 403
 404
 405
 406
 407
 408
 409
 410
 411
 412
 413
 414
 415
 416
 417
 418
 419
 420
 421
 422
 423
 424
 425
 426
 427
 428
 429
 430
 431
 432
 433
 434
 435
 436
 437
 438
 439
 440
 441
 442
 443
 444
 445
 446
 447
 448
 449
 450
 451
 452
 453
 454
 455
 456
 457
 458
 459
 460
 461
 462
 463
 464
 465
 466
 467
 468
 469
 470
 471
 472
 473
 474
 475
 476
 477
 478
 479
 480
 481
 482
 483
 484
 485
 486
 487
 488
 489
 490
 491
 492
 493
 494
 495
 496
 497
 498
 499
 500
 501
 502
 503
 504
 505
 506
 507
 508
 509
 510
 511
 512
 513
 514
 515
 516
 517
 518
 519
 520
 521
 522
 523
 524
 525

Table of Contents

Abstract.....	iii
Table of Contents.....	iv
Figures & Tables	v
List Abbreviations & Symbols	vi
Technical report.....	1
1 Intro to Second Harmonic Generation	1
2 Neat Liquids.....	2
3 Monolayers at the Air/Water Interface	3
4 Liquid/solid and Electrified Interfaces	19
5 Dynamics at the Air/Water Interface.....	24
6 Femtosecond Studies of Electrons in Liquids.....	30
7 Picosecond Studies of Chemical Intermediates.....	39
References.....	45
Personal Data.....	48

List of Figures and Tables

Figure 1.1 Surface Second Harmonic Set-up.....	2
Figure 3.1 p-Nitrophenol	4
Figure 3.2 Acid-base equilibrium of p-hexadecyl aniline.....	5
Figure 3.3 SH field versus bulk pH.....	7
Figure 3.4 Surface Phase Diagram for 4 monolayer systems.....	9
Figure 3.5 SH Fluctuations versus time.....	10
Figure 3.6 Probability Density Function.....	12
Figure 3.7 Autocorrelation Function for SH Signal versus time.....	13
Table 1 Correlation time versus Area per Molecule and Laser Spot Size	16
Figure 3.8 Orientation Fluctuation	18
Figure 4.1 Fraction of SiONa versus bulk pH.....	21
Figure 5.1 Photoisomerization of DODCI (3,3'-diethyl- oxydiacarbocyanine iodide)	25
Figure 5.2 Proton transfer in aminopyrene	26
Figure 5.3 Proton transfer in PNP	26
Figure 5.4 Rotational Motion at the Air/Water Interface	28
Figure 6.1 Electron Solvation Dynamics in Neat Water	32
Figure 6.2 Wet Electron Absorption Spectra	33
Figure 6.3 Geminate Recombination in Water and D ₂ O	35
Figure 6.4 Geminate Recombination in iso-octane	37
Figure 6.5 Geminate recombination in n-octane	38
Figure 7.1 Two anthracene endoperoxides.....	40
Figure 7.2 Two anthracene endoperoxides.....	40
Figure 7.3 Biradical mechanism for photofragmentation of aromatic endoperoxides	41
Figure 7.4 Dimesitylcarbene (DMC).....	42
Figure 7.5 Photoisomerization of stilbene.....	43
Figure 7.6 Schematic of equilibrium between tight and loose stilbene/cyclodextrin complexes.....	44

List of Symbols and Abbreviations

A	surface area
E	electric field
K_{eq}	equilibrium constant
P	electric polarization
PNP	p-nitrophenol
SH	second harmonic
SHG	second harmonic generation
SSHG	surface second harmonic generation
T	temperature in degrees Kelvin
a_x	activity of the species x
f_x	fraction of the species x
k	Boltzmann's constant
pH ^s	pH at the surface
pK ^s	pK at the surface
Å	Angstrom (10^{-8} cm)
ΔG_{ABS}	Gibb's Free energy of absorption
α_{ijk}	the polarizability tensor
χ_{ijk}	the susceptibility tensor
Φ	surface potential
$\Omega(t)$	Euler angles (θ, ϕ, ψ) as a function of time
ϵ	absorption coefficient or dielectric constant
ϕ	phase of the electric field
π	surface pressure (dyne/cm ²)
ω	frequency of the light field

AFOSR Final Technical Report

1. Introduction to Surface Second Harmonic Generation

1.1 theory Optical nonlinearities occur in media exposed to very high light fluxes, such as those associated with lasers. One of the nonlinear optical effects is second harmonic generation (SHG). The physical interpretation of SHG is that a laser beam at frequency ω interacts with a nonlinear medium and generates a nonlinear polarization. The latter being a collection of oscillating dipoles acts as a source of radiation at 2ω [1]. The key feature of SHG that makes this experiment feasible is that SHG is electric dipole forbidden in the bulk but allowed at the interface where the symmetry is broken [2,3]. Thus SHG can be used to probe selectively the interface layer.

The second harmonic polarization is proportional to the second-order nonlinear susceptibility of the surface $\chi^{s(2)}$,

$$P_i(2\omega) = \chi_{ijk}^{s(2)} E_j(\omega) E_k(\omega) \quad (\text{eq 1.1})$$

In the experiment, the specific elements of the surface nonlinear susceptibility can be measured, which are directly related to the population of the molecules at the surface, N_s , and the nonlinear polarizability of the molecule, $\alpha^{(2)}$ averaging over the orientational distribution at the surface.

$$\chi_{ijk} = N_s \langle \alpha_{ijk}^{(2)} \rangle \quad (\text{eq 1.2})$$

Therefore, second harmonic generation can give information about molecular population and molecular orientation at the surface.

1.2 experimental method The experimental arrangement that we use in our SH studies is schematically shown below.

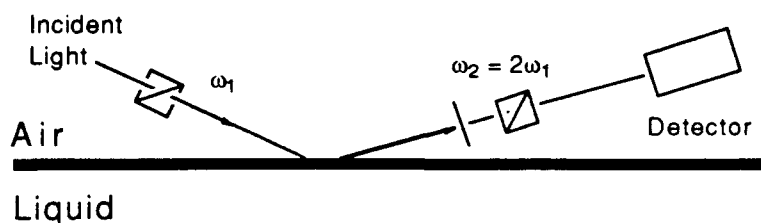


Figure 1
Surface Second Harmonic Experimental Setup

The magnitude of the second harmonic signal is proportional to the square of the population of species at the interface. By measuring the polarization of the second harmonic light, the orientation of the molecules at the interface can be inferred.

2. Interfacial Studies of Neat Liquids

2.1 The Role of Hydrogen Bonding on the Orientation of Molecules at the Neat Air/Liquid Interface Expanding on our results obtained for neat water, we examined other neat solvent systems in order to sort out the relative contribution to the orienting force made by the dipole-dipole interaction, ionic interaction, hydrogen bonding effects as well as entropy effects due to the presence of a hydrocarbon chain. Assuming an "up" versus "down" model, the nonlinear susceptibility could be related to the net orientation of the molecules.[4]

In examining a series of neat liquids we found that, in terms of the temperature effects, that the solvents could be grouped into two broad classes (hydrogen-bonding and non-hydrogen bonding solvents). We found for hydrogen bonding liquids that the SH signal exhibited a strong temperature dependence, where the surface sensitive signal decreased with increasing temperature. This is to be contrasted with non-hydrogen bonding liquids, where there was a negligible temperature effect. Our results are easily explained by considering that there is a strong orientating field of the surface molecules, due to the effects of hydrogen bonding. When temperature rises, more and more hydrogen bonds break, diminishing the orienting force, which thus causes the SH signal intensity to drop.

Hydrophobic effects was also found to strongly affect molecular orientation at the air/liquid interface. Specifically, our SHG studies on a

homologous series of alcohols show that the hydrocarbon chain has a large influence on the interfacial molecular orientation, as evidenced by the SH signal enhancement obtained when switching between water and methanol, while from methanol to octanol the SH signal does not change significantly. If one assumes a simple "up" versus "down" orientation model, we found that only one methylene, i.e., methanol, is enough to favor one orientation to the other. Namely, that the hydrocarbon portion of the molecule tends to favor the "up" orientation (toward the air). This important result is also independently confirmed by surface tension measurements.

2.2 Energetics of Orientation of Water Molecules at the Vapor/Neat Water Interface

In an earlier study we concluded that the preferred orientation of water molecules at the interface is the protons toward the bulk water. To study the energetics of the preferred orientation of "up" vs. "down" we measured the temperature dependence of the SH signal. Using a simple model of the orienting forces at the interface, similar to that of a system of permanent dipoles in an external field, we obtained an energy of orientation of 280 ± 80 cal/mole at 295 °K, i. e. about 1/2 kT at room temperature.

3. Studies of Monolayers at the Air/Water Interface Using Second Harmonic Generation

3.1 Effects of Long Chain Molecules on the Population and the Orientation of Organic Molecules at the Air/Water Interface

Determining the nature and the effect of co-adsorption of chemically different solute molecules at the air/liquid interface is a fundamental issue. It also has direct and immediate impact on our ability to understand how the presence of one adsorbed molecule can influence the interfacial population and orientation of another. In order to address this issue, we have considered how a lipid monolayer can influence the ability of a molecule in the aqueous subphase to "penetrate" into the lipid-rich liquid/air interface region.[5] We were further motivated to consider this particular study since it has direct bearing on the nature of transport across membranes and bilayers, as well as on our interest in developing novel two-dimensional materials. Previous studies have been hampered in yielding detailed information on this problem since the techniques available (such as surface tension measurements) could not discriminate

between the different solute molecules in the interface. With the SHG method we do have the resolving power to discriminate and determine what is at the interface.

It was found that a fatty acid monolayer has a profound influence on the penetrating ability of a solute. Using p-nitrophenol (PNP) as the surface-active solute we saw that its surface population is dramatically enhanced as the lipid density is increased (reaching a maximum at approximately 50 \AA^2 per molecule for the lipid density). This was found when either pentadecanoic acid (a 15 carbon chain acid) or hexadecanoic acid (a 16 carbon chain acid) was used as the insoluble fatty acid lipid. We interpret this enhancement in the

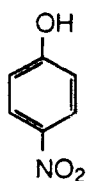


Figure 3.1
p-Nitrophenol (PNP)

PNP population as resulting from the preferential solubilization of PNP by the lipid in the lipid rich interface. It is pointed out that at still higher lipid densities we see that there is a reversal in the PNP population dependence on lipid surface density. The turn-over occurs when the fatty acid lipid density exceeds about $50 \text{ \AA}^2/\text{molecule}$. From independent measurements we know that the fatty acid monolayer becomes close packed (more ordered) when its surface density is increased. The critical area of $50 \text{ \AA}^2/\text{molecule}$ for the lipid above which the PNP molecule population decreases is due to the fact that the available surface area is smaller than is needed for which a PNP molecule can reside. In other words, as the lipid monolayer becomes close packed it "squeezes" out the moderately sized PNP molecule from the surface. In light of the dramatic influence of the lipid monolayer on the composition of the co-adsorbed solute PNP, we expect that the monolayer should also influence the orientation of the solute as well. In confirmation of this idea, we found that at low monolayer densities (in the limit for which there is an enhancement in co-solute population) the PNP orientation does not change significantly from its nominal value of $60\text{--}63^\circ$. Above the critical lipid density of $50 \text{ \AA}^2/\text{molecule}$ (in the limit where the lipid

is close packed and there is concomitant diminution in the PNP population) we find that the molecular orientation of PNP flips up more toward the surface normal. At 25 Å² per molecule we determined the molecular angle of PNP to be 51°.

3.2 Measurement of pH and pK_a at the Air/Water Interface We want to investigate the effect of asymmetric forces at the interface on an equilibrium constant like pK_a. SHG is used to measure the relative population of the acid and base at the interface. Consider the acid-base equilibrium at the surface for the insoluble material p-hexadecyl aniline,

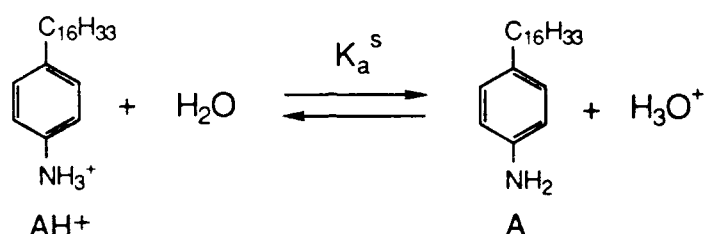


Figure 3.2
Acid-base equilibrium of p-hexadecyl aniline

The pK_a^S for the above equilibrium,

$$\text{pK}_a^S = \text{pH}^S + \log \frac{N_{\text{HA}^+}}{N_{\text{A}}} \quad (\text{eq 3.1})$$

s denotes the properties at the surface and N_A and N_{HA}⁺ are the number densities (molecules/cm²) of aniline and anilinium at the surface respectively. To obtain the pK_a one needs to know apart from the concentration of the acid and base forms, the hydronium ion concentration at the surface. The surface pH is related to bulk pH through the surface potential Φ by the following relation,

$$\text{pH}^S = \text{pH}^b + \frac{e\Phi}{2.3RT} \quad (\text{eq 3.2})$$

The surface potential Φ can be determined using the Gouy Chapman model of electrical double layers [6,7] as

$$\Phi = \frac{2kT}{e} \sinh^{-1} \left(eN_{HA^+} \sqrt{\frac{\pi}{2C\epsilon kT}} \right) \quad (\text{eq 3.3})$$

where C is the total number of ions/cm³ in bulk, ϵ the dielectric constant of the medium, T the temperature in kelvin, k the Boltzmann constant and e the electronic charge. To calculate the surface potential from the Guoy-Chapman model the surface population of the charged form (acid or base), obtained from the SH measurement is used. We thus obtain for such a system a total SH electric field

$$E_{\text{tot}} = \frac{N_A}{N_0} E_A e^{i\phi} + \frac{N_{HA^+}}{N_0} E_{HA^+} = \frac{N_A}{N_0} E_A e^{i\phi} + \left(1 - \frac{N_A}{N_0} \right) E_{HA^+} \quad (\text{eq 3.4})$$

where $N_A + N_{HA^+} = N_0$ is the total number of molecules at the surface which is known by virtue of spreading known concentration solution. E_A is the SH electric field of aniline at a sufficiently high pH where $N_A = N_0$, similarly E_{HA^+} is that of anilinium at a sufficiently low pH where $N_{HA^+} = N_0$, and ϕ is the phase difference between SH electric field of the two species.

Note that the measurement of the SH signal E_{tot} vs. bulk pH can be transformed into $\frac{N_A}{N_0}$ or $\frac{N_{HA^+}}{N_0}$ vs. bulk pH, since E_{tot} , E_A , E_{HA^+} and ϕ are measured independently using SHG. The data are fitted to eqs. 1,2,3,4 allowing the pK_a^S to be the only adjustable parameter. The resulting fit is shown as a solid line in figure 3.3. The value of pK_a obtained in this way is 3.6 ± 0.2 . pK_a in the bulk for a long chain aniline is 5.3 units at ionic strength of 1N. Thus a difference of 1.7 units in pK_a corresponding to fifty times increase in the acidity is observed. This increase in acidity arises from the higher free energy of a charged species at the air/water interface, shifting the anilinium acid-base equilibrium towards the energetically more favorable neutral form. This is a direct evidence that the chemical properties such as equilibrium constants and pH at surface can differ significantly.

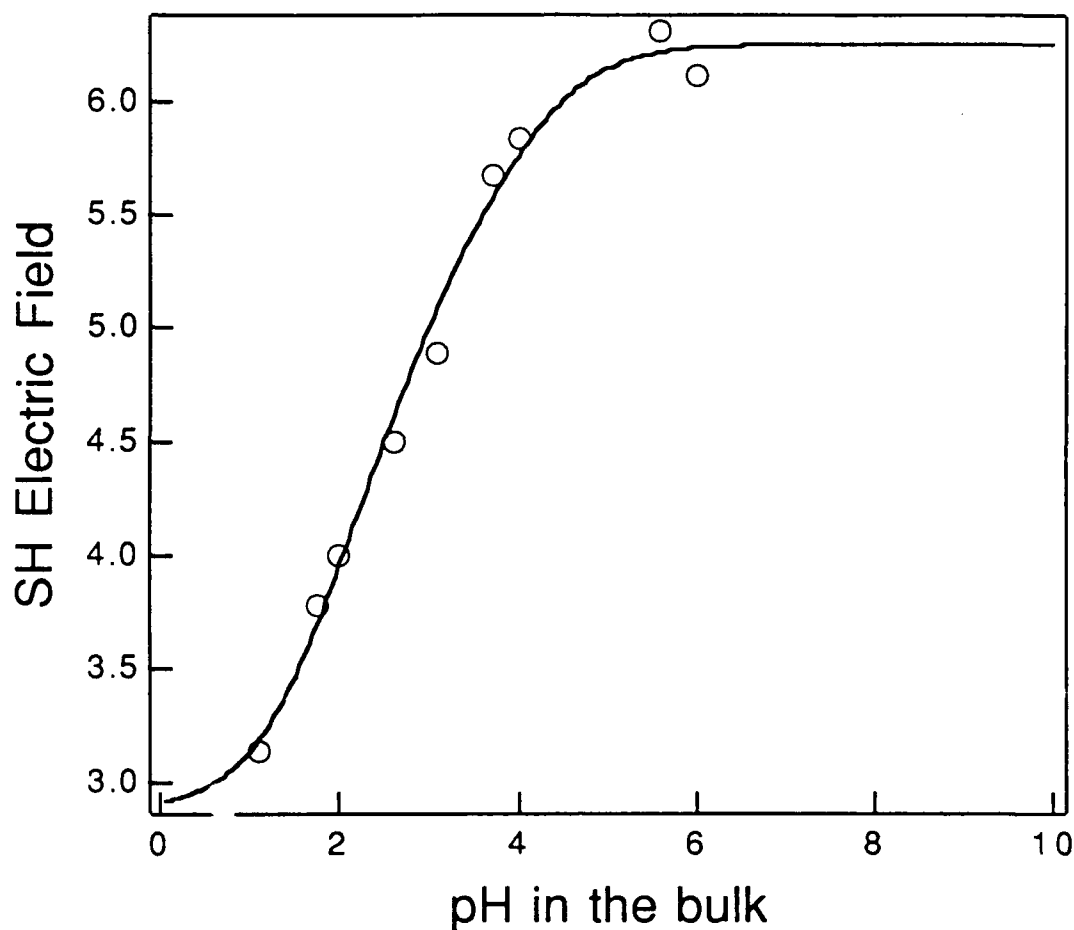


Figure 3.3

SH electric field as a function of bulk pH at constant ionic strength of 1M . Solid curve represents the fit using Gouy-Chapman model.

3.3 Study of surface diffusion by SH fluctuations Insoluble film (monolayer) at the air/water interface is a typical two dimensional system. Analogous to three dimensional systems, these insoluble films exist in solid, liquid and gas phases depending on the density of the molecules at the surface. However, the gas-liquid coexistence region is of particular interest with regard to the nature of phase transition, structure of the coexisting phases and the dynamics of the motion at the surface of the different phases. This coexistence region has been studied extensively using a wide variety of techniques, but the

results from different experiments are not in agreement with each other resulting in a lot of controversies.[8-11] Hence we want to use SHG to investigate surface heterogeneity in the gas-liquid coexistence region.

A heterogeneous surface in the gas-liquid region consists of two different types of molecular arrangements. In one configuration, the molecules are clustered together at a density corresponding to a liquid-like surface phase. In the other arrangement, the molecules are sufficiently far apart so that there are no interactions between individual molecules; this corresponds to a gas-like phase of the molecules at the surface. In the coexistence region, the surface is heterogeneous in having regions of liquid clusters and regions of gas, interspersed among each other. The liquid phase gives rise to high signal whereas gas phase gives small signal and hence the time dependent fluctuations in the SH signal is used to investigate the motion of these liquid clusters into and out of the probe area. The system we have studied is hexadecyl aniline spread on water at coverages corresponding to the gas-liquid coexistence region. The surface pressure vs area phase diagram is shown in figure 3.4, next page.

The measured SH signal $I(t)$ at time t is related to A_l and A_g , the fraction of the area under observation covered by liquid and gas phases respectively, as

$$I(t) = I_l A_l + I_g A_g = (I_l - I_g) A_l + I_g \quad (\text{eq 3.5})$$

I_l and I_g are the signal from homogeneous liquid and gas phase respectively. We then define $\Delta I(t) = I(t) - \langle I \rangle$, where $\langle I \rangle$ is the average signal, and obtain a correlation function,

$$\langle \Delta I(0) \Delta I(t) \rangle = (I_l - I_g)^2 \langle \Delta A_l(0) \Delta A_l(t) \rangle \quad (\text{eq 3.6})$$

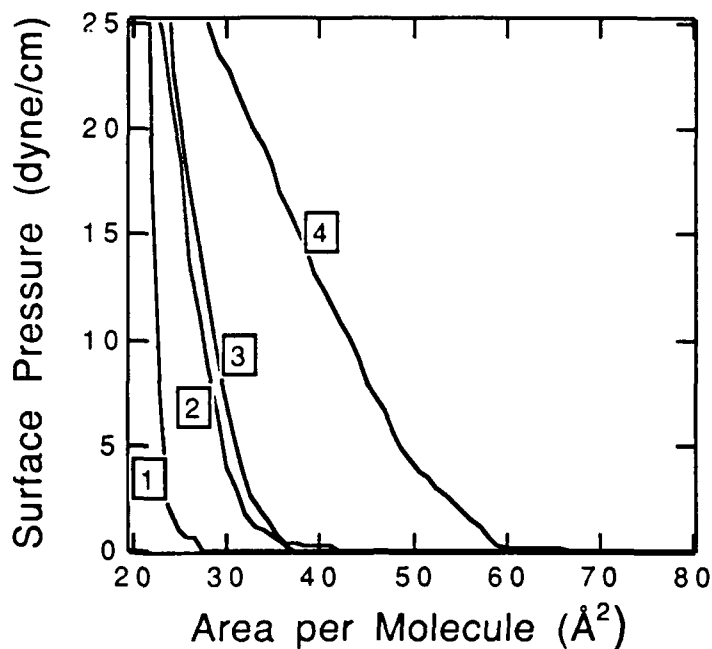


Figure 3.4

Phase Diagram for 4 monolayer systems

1 C16-phenol/water; 2 C-16-aniline/water;

3 C-18-phenolate/2N KOH; 4 C16-anilinium/1N HCl

The time dependence arises from the changes in the fraction of the area covered by the liquid phase. Assuming the cluster size to be invariant, the changes can be attributed to the number density fluctuations of the liquid clusters.

The characteristic time of decay of the correlation function is thus related to the time that a cluster of liquid remains within the beam. If the cluster motion is diffusive, a diffusion constant may be estimated using the results for random walk in two dimensions, $\langle r^2 \rangle = 4Dt$, where r is a characteristic length, in this case the beam radius ($\sim 3 \mu\text{m}$), and t is the decay time of the observed intensity fluctuations.

The SH intensity was recorded every 0.5 s for half an hour. p-nitrophenol solution is used as the subphase as it is a good probe of the surface generating large SH signal. Experiments were performed at 37, 50, 100, 200 and 400 $\text{\AA}^2/\text{molecule}$ of C16 aniline. The results are shown in figure 3.5, next page.

SH Signal

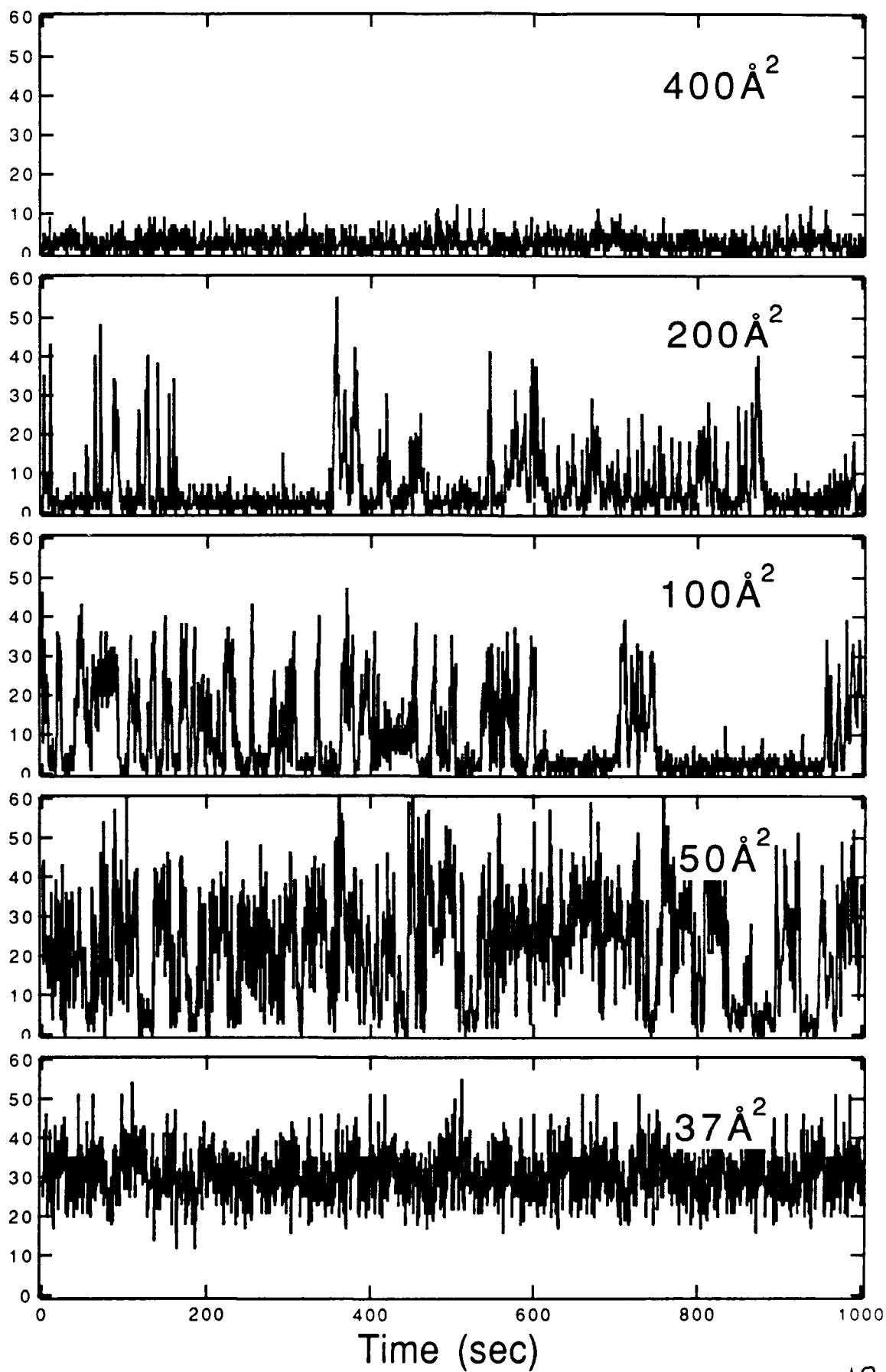


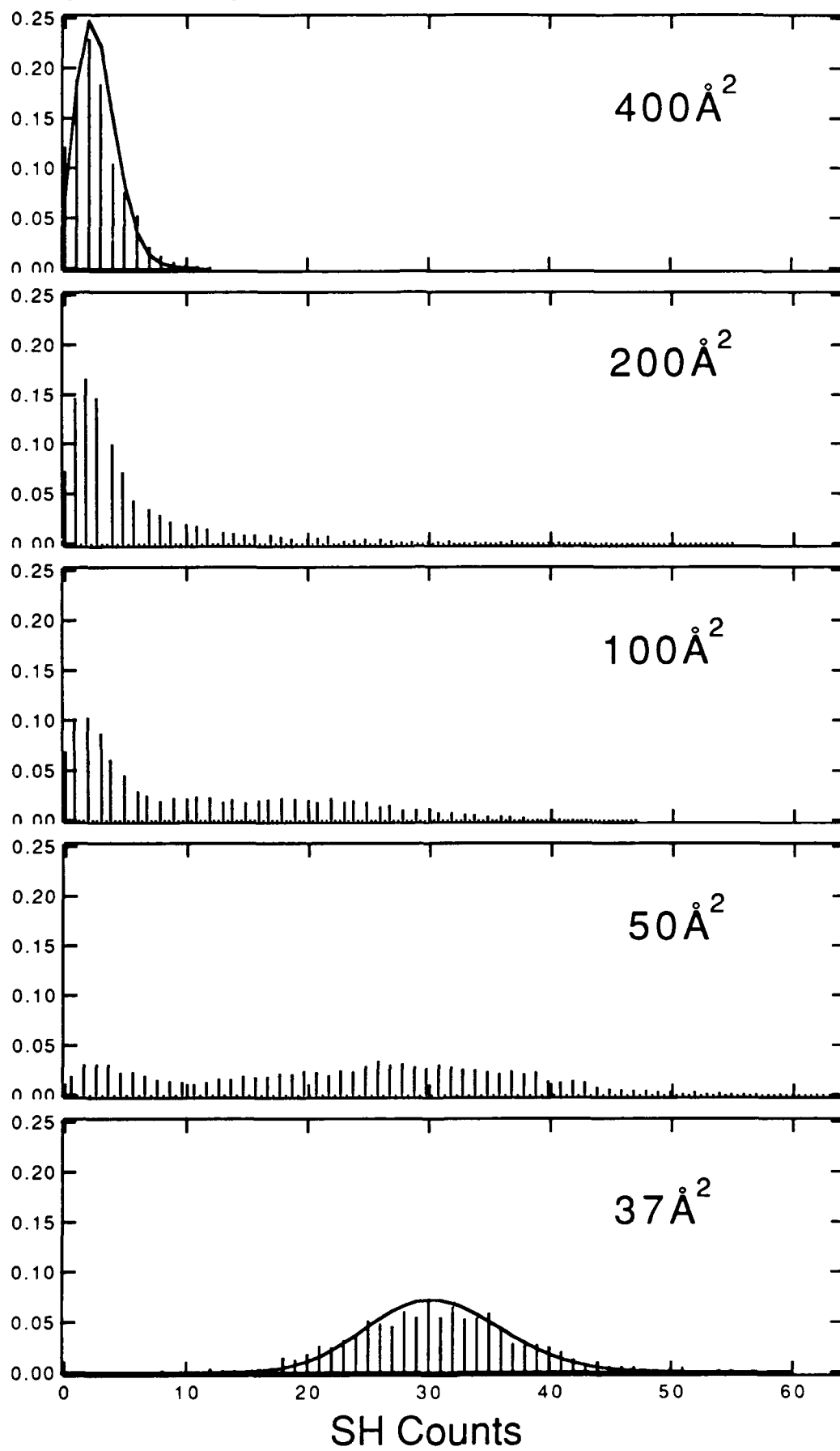
Figure 3.5

The fluctuations in the SH signal from 400\AA^2 and $37\text{\AA}^2/\text{molecule}$ is different from that generated by the C16 aniline at coverages of 400, 200 and $100\text{\AA}^2/\text{molecule}$. This can be understood in terms of the phase diagram. At $37\text{\AA}^2/\text{molecule}$ the C16 aniline on the surface is in a homogeneous liquid-like phase, while the other three measurements correspond to its being inside the gas-liquid coexistence region. At very low coverages ('gas'), the SH signal is the same as for a bare water surface. However, as the C16 aniline packing is increased, a substantially larger SH signal is generated. It is notable that the 'low' signal in 200\AA^2 is the same signal as 400\AA^2 . This signal corresponds to patches of the surface with the low density gas-like coverage in the irradiated region. The 'high' signals, on the other hand, correspond to the high density 'liquid'-like coverage in the irradiated region. At $200\text{\AA}^2/\text{molecule}$ the coverage is low, and there are few liquid-like islands dispersed in gas-like coverage. As the packing is increased, at 100 and $50\text{\AA}^2/\text{molecule}$, more 'high' signals are obtained, corresponding to a higher fraction of the C16 aniline in a liquid-like state. Finally, at $37\text{\AA}^2/\text{molecule}$, the surface is now covered by a homogeneous layer of palmitic acid in its 'liquid-like' phase. The signal fluctuations for both the gas phase surface 400\AA^2 and the homogeneous liquid 37\AA^2 are ascribed to random noise as discussed below.

As a further test of the significance of the observed fluctuations, the probability density function for our data was plotted in figure 3.6. The probability density functions of 400 and 37\AA^2 have been fit to a poisson distribution which shows that fluctuations observed in these cases is random noise, arising from a homogeneous surface. However the distributions in 200, 100, 50\AA^2 do not look like simple ones and can probably be fitted to a linear combination of poissos, which is consistent with the notion of a heterogeneous surface.

The autocorrelation $\langle \Delta I(0) \Delta I(t) \rangle$ vs. time are shown in figure 3.7. The data for 50, 100 and $200\text{\AA}^2/\text{molecule}$ show, a monotonic decay in the correlation function while those for 400 and 37\AA^2 show only a delta function indicating a randomly uncorrelated noise.

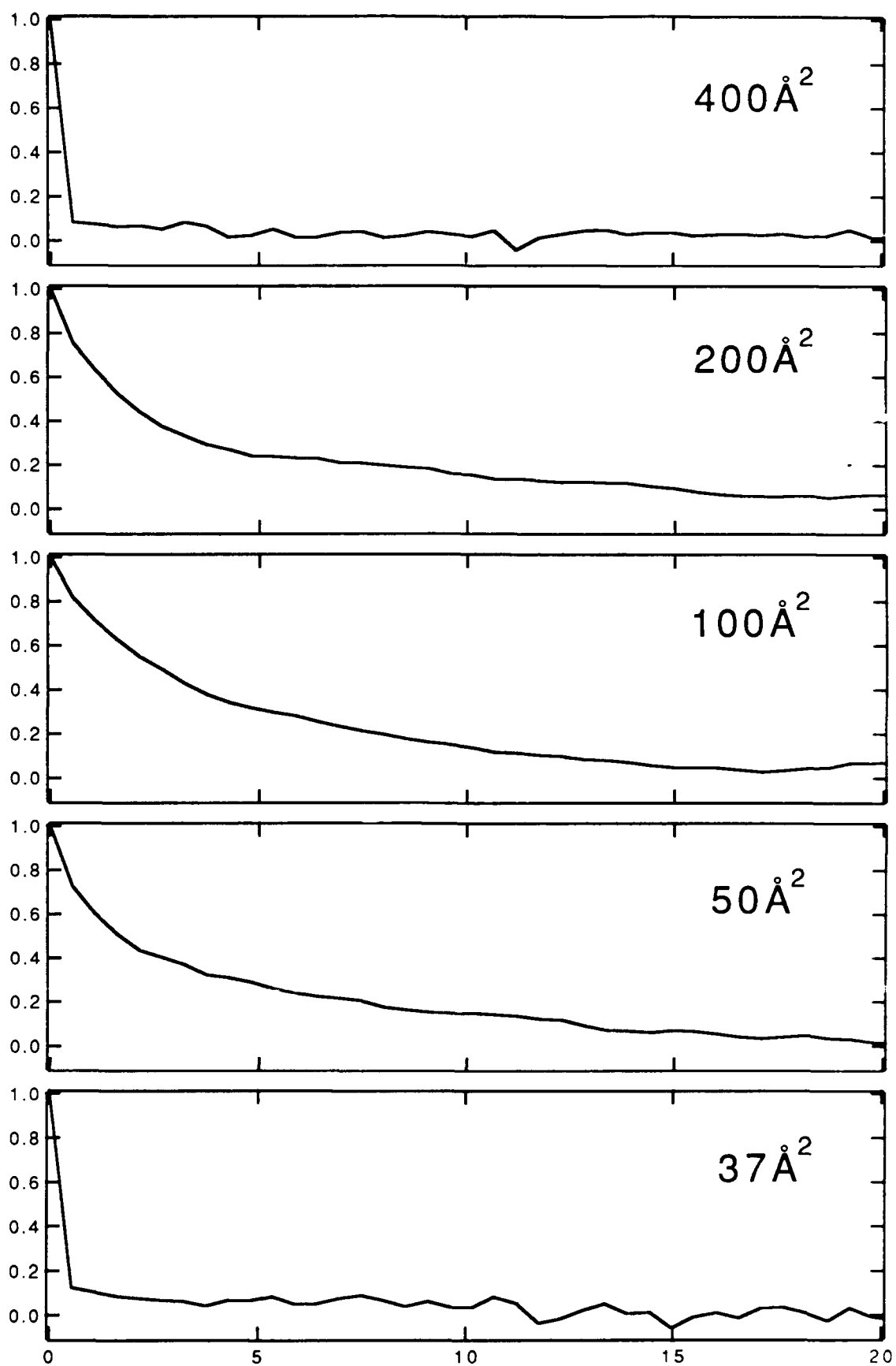
Probability Density Function



SH Counts

Figure 3.6

Autocorrelation Function of ΔI



Time (sec)

Figure 3.7

Since the high signals obtained for 50, 100, and 200 Å²/molecule, i.e., in the coexistence region, are of the same magnitude as the signal obtained for the pure liquid state e.g. at 37 Å²/molecule, we conclude that the clusters are comparable in size with our incident beam. By fitting our data to a diffusion model, a diffusion constant of $\sim 10^{-8}$ cm²/s and a size of $\sim 1 \mu\text{m}$ are obtained.

3.4 Orientation Phase Transition Studied by SH Fluctuation

We now wish to report the observation of orientational fluctuations of lipid molecules at the air/water interface, which we attribute to a heretofore unknown orientational phase transition. These fluctuations were shown to be orientational by the observations that they depended on the polarization of the incident light field and the polarization of the second harmonic light field that was detected. The experimental results of this study bear on the organization of lipid molecules at the air/water interface, a subject that has been and remains one of intense experimental and theoretical activity. The molecule we studied is hexadecylaniline, a long chain aniline where the aniline head group has C_{2v} symmetry. For an interface that is isotropic in the surface plane, i.e. is rotationally invariant with respect to the interface normal, populated by molecules of C_{2v} symmetry the explicit relation between $\chi^{(2)}$ and $\alpha^{(2)}$ yields for two of the $\chi^{(2)}$ elements that we will be concerned with the following expressions,

$$\chi_{zxx}^{(2)} = \frac{1}{2} N_s [f(\alpha_{zzz}^{(2)}, \alpha_{zxx}^{(2)}, \alpha_{xzx}^{(2)}, \theta, \psi) + \alpha_{zxx}^{(2)} \langle \cos \theta \rangle] \quad (\text{eq 3.7a})$$

$$\chi_{xzx}^{(2)} = \frac{1}{2} N_s [f(\alpha_{zzz}^{(2)}, \alpha_{zxx}^{(2)}, \alpha_{xzx}^{(2)}, \theta, \psi) + \alpha_{xzx}^{(2)} \langle \cos \theta \rangle] \quad (\text{eq 3.7b})$$

where N_s is the lipid surface density (molecules/cm²) and

$$f(\alpha_{zzz}^{(2)}, \alpha_{zxx}^{(2)}, \alpha_{xzx}^{(2)}, \theta, \psi) = \alpha_{zzz}^{(2)} \langle \cos \theta \sin^2 \theta \rangle - (\alpha_{zxx}^{(2)} + 2\alpha_{xzx}^{(2)}) \langle \cos \theta \sin^2 \theta \sin^2 \psi \rangle, \quad (\text{eq. 3.8})$$

θ is the angle between the molecular symmetry axis z and the surface normal Z , and ψ is the rotation angle of the molecule about its symmetry axis z . From Eqs. 3.7 and 3.8 we see that $\chi_{xzx}^{(2)}$ and $\chi_{zxx}^{(2)}$ differ only in the nonlinear polarizability coefficients of $\langle \cos\theta \rangle$.

The SH signal corresponding to these two elements, $\chi_{xzx}^{(2)}$ and $\chi_{zxx}^{(2)}$ (Eqs 3.7 and 3.8), were measured as a function of time. On further compression to densities above 37 \AA^2 where the monolayer is in the homogeneous liquid phase region, a non-Poisson fluctuations were observed when $\chi_{xzx}^{(2)}$ is measured. However, for $\chi_{zxx}^{(2)}$ element, the fluctuations observed were very close to a Poisson distribution. We therefore conclude that we are detecting a polarization dependent and hence an orientational fluctuation. It should be noted that there is no indication from the π -A phase diagram of a phase transition in this density region of the liquid phase. On compressing the monolayer further we find that fluctuations decrease and at 28 \AA^2 the fluctuations are approximately Poisson in character. We were unable to go to higher coverages because of the collapse of the monolayer below 28 \AA^2 .

We now consider the basis for the orientational fluctuations. Since the SH signal is due chiefly to aniline we note that the fluctuations that we observe must be due to the fluctuations in the orientation of the aniline head group. However one cannot conclude from this that the driving force for these fluctuations are due only to head group interactions, e.g. via a dipole-dipole coupling between the head groups. It is quite reasonable that chain-chain interactions at these relatively high densities play some role in driving the head group orientational phase transition. We know that the chain-chain interactions cannot be the sole factor however since we do not observe any orientational fluctuations for an equal chain length lipid with a different head group, namely hexadecylphenol ($n\text{-C}_{16}\text{H}_{33}\text{-C}_6\text{H}_5\text{OH}$).

Let us now consider the orientation of the aniline head group, which is defined by θ , the angle of the aniline symmetry axis with the interface normal Z and ψ the angle of twist about the aniline symmetry axis. Noting that ψ is

present only in the function $f(\alpha_{zzz}^{(2)}, \alpha_{zxx}^{(2)}, \alpha_{xzx}^{(2)}, \theta, \psi)$ for $\chi_{xzx}^{(2)}$ and $\chi_{zxx}^{(2)}$, Eqs.

3.7 and 3.8, it appears that the θ dependence in the $\alpha_{xzx} \langle \cos \theta \rangle$ term is responsible for the fluctuations, since it is only this term that differs for $\chi_{xzx}^{(2)}$ and $\chi_{zxx}^{(2)}$. From theoretical estimates $\alpha_{xzx}^{(2)}$ is much larger than $\alpha_{zxx}^{(2)}$ for aniline.

This would explain why we readily observed orientational fluctuations in the $\chi_{xzx}^{(2)}$ element and not in the $\chi_{zxx}^{(2)}$ element.

In order to examine the spatial range of the orientational fluctuation we varied the laser beam area by a factor of four from a radius of $3\mu\text{m}$ to $6\mu\text{m}$. The results of autocorrelation times for the two beam areas for various monolayer coverages is given in Table 1.

	36\AA^2	34\AA^2	32\AA^2	30\AA^2	28\AA^2
$3\mu\text{m}$	9	13	16	17	~ 16
$6\mu\text{m}$	5	8	12	17	~ 15

Table 1.
Correlation Time t_c (sec) Dependence of Area per Molecule
and Observation Spot Size

As the laser spot size is increased the number of domains viewed increases, and therefore a more rapid decorrelation would be expected. As the transition point is approached the domains increase in size and the decay of the autocorrelation function would be slower, though still showing a change with spot size. At 30\AA^2 the system is near the transition point and the domains are very large, becoming larger than the beam size. This is seen in the result that the same decay time is observed for the 3μ and 6μ radii beam, which indicates that the orientational correlation length is greater than 6μ . If the transition was second order then this correlation length would diverge at the transition point. Based on these scaling experiments, which indicate a long correlation length,

we infer that the phase transition is likely to be weak first order if not second order.

As alluded to earlier the importance of chain-chain interactions on the observed orientational fluctuations is seen in the strong dependence of the SH fluctuations on the chain length of the aniline lipid. The autocorrelation functions and probability density functions of $\chi_{\text{ZZX}}^{(2)}$ for the C12, C14, C16 anilines at a coverage of 34\AA^2 are shown in figure 3.8. It is evident from figure 5 that the shorter chain anilines have shorter correlation times and distributions closer to Poisson, thus indicating a more homogeneous surface on the time scale of our measurements. In fact C12-aniline does not show any deviation from Poisson fluctuation for the experimental sampling time scale of 0.5 sec that we use. This could be due to a correlation length that is much smaller than the laser beam area (3μ radii), and/or a relaxation that is much faster than the 0.5 sec sampling time. It is perhaps not surprising that the stronger attractive interactions for the longer chain anilines would be more restrictive of the head group orientational motions.

To examine the effect of the head group on these orientational fluctuations we studied C14, C16 and C18-phenols as well as C16 anilinium and C18 phenolate system. Although phenol and aniline have similar dipole moments, and the chain lengths were the same for both the aniline and phenol lipids we observed no orientational fluctuations for any of the phenols. The observation indicates that the interactions of the head groups with the surrounding water molecules is an important factor, recognizing that the hydrogen bonding properties of the aniline vs phenol are different. The necessary balance between the various forces, chain-chain, hydrogen bonding, and electrostatic, involved in the phase transition is demonstrated by our observation that the charged lipid C18-phenolate ($\text{C18-C}_6\text{H}_5\text{O}^-$) manifests orientational fluctuations similar to the C16-aniline. The charged anilinium lipids ($\text{C16-C}_6\text{H}_5\text{NH}_3^+$) and as noted earlier the neutral phenol lipids do not show orientational fluctuations. It is of interest that the neutral and charged lipids showing these fluctuations have similar π -A phase diagrams.

Autocorrelation Function of ΔI

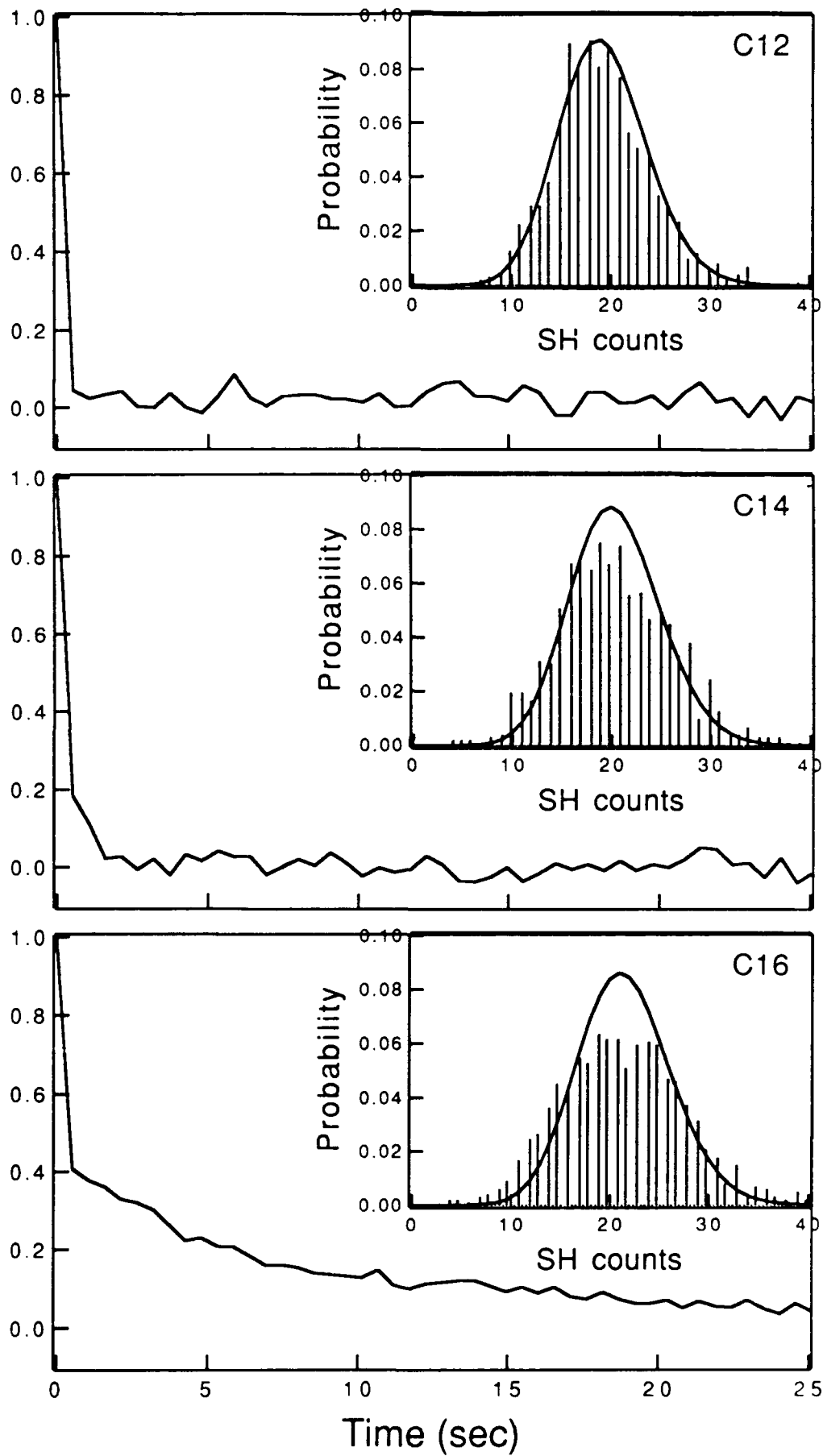
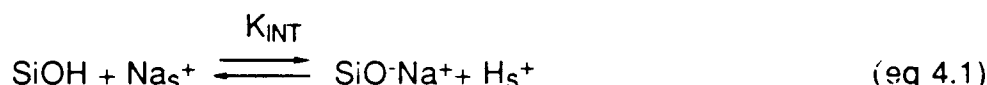


Figure 3.8

4. Solid-Liquid and Electrified Interfaces

4.1 Studies of Silica/electrolyte solution interface by SHG The glass-water interface is an important example of a solid-liquid interface. In the case of silica in contact with electrolyte solution, such as NaCl, the surface complexation dominates at higher electrolyte concentration [12,13]. Thus, the main surface reaction at silica/electrolyte (NaCl) solution is



With the intrinsic surface equilibrium constant

$$K_{\text{INT}} = \frac{f_{\text{SiOH}} a_{\text{Na}^+}}{f_{\text{SiONa}} a_{\text{H}^+}} \exp[-e(\Psi_0 - \Psi_\beta)/kT] \quad (\text{eq 4.2})$$

Where SiO^-Na^+ is an ion pair complex, simplified as SiONa , while f_{SiOH} , f_{SiO^-} and f_{SiONa} are the fraction of SiOH , SiO^- and SiONa , respectively, a_{H^+} and a_{Na^+} are activities of proton and sodium ion, respectively. Ψ_0 is the electrostatic potential affecting the SiO^- charge sites, which are assumed to be located in the same zero plane as that for H^+ and OH^- . Invoking the Stern model of an electrified interface, the role of counterions is included in the potential Ψ_β .

The basic features of the SH signal from silica/electrolyte interface are that at fixed ionic strength, the SH signal increases with increasing pH, while at fixed pH, SH signal decreases with increasing concentration of NaCl. It is well known that surface silanols dissociate more and more with increasing pH and that there is more surface complexation with increasing concentration of NaCl. Thus, we may conclude that the SH signal from silica/electrolyte interface increases with increasing total surface charge density ($N_{\text{SiO}^-} + N_{\text{SiONa}}$) and that at the same surface charge density, the SH signal decreases with more surface complexation. The SH signal may arise from two different mechanisms, either from the second order hyperpolarizability or the third order hyperpolarizability

arising from the electrical potential across the solid/liquid interface due to the surface charge [1,14], or combination of both.

At higher electrolyte concentration, surface complexation dominates and the amount of SiONa is much larger than that of SiO⁻, e. g. $f_{\text{SiONa}} \gg f_{\text{SiO}^-}$. Under this condition, the two different mechanisms end up with the identical relationship between the SH signal and the density of the surface charge species, e.g. SiO⁻ and SiONa. It was found that at a given pH, the fraction of SiONa, f_{SiONa} is

$$f_{\text{SiONa}} = \frac{(I_s)^{1/2} - (I_s(\text{pH}=2))^{1/2}}{(I_s(\text{pH}=13))^{1/2} - (I_s(\text{pH}=2))^{1/2}} \quad (\text{eq 4.3})$$

Where $(I_s)^{1/2}$, $(I_s(\text{pH}=2))^{1/2}$ and $(I_s(\text{pH}=13))^{1/2}$ are the square roots of the SHG intensity, respectively. This is not surprising since the surface complexation dominates and the net charge density in diffuse layer is very small compared to the charge density at the zero plane, which is linearly proportional to E_0 , the electric field at the interface. It is thus fortunately that we can obtain unique results of equilibrium constants of surface reaction (eq. 4.1) by fitting the experimental data even if we could not separate these two different mechanisms, although it is of importance and interest to separate them. An attempt to separate these two mechanisms by varying the temperature is in progress.

Knowing the fraction of the ion-pair complexes SiONa, f_{SiONa} from the experimental measurement according to eq. 4.3, we can determine the intrinsic surface complexation constant K_{INT} of reaction 4.1. The plot of f_{SiONa} vs bulk pH looks like a titration curve with two pK_a values. This suggests that there are two different exchange sites with distinct intrinsic equilibrium constants K_{INT} . Thus, a two-site ion exchange model proposed by Allen et al [15] was adopted to analyze our data. The two-site model assumes that two distinct types of silanol groups (I and II) are available, and that the intrinsic surface complexation constants K_{INT} differ so much that the type sites I first filled completely, and that only then do the type II sites fill.

The result is shown in following figure 4.1. It was found that about 20% of the surface silanols have a $\text{pK}_{\text{INT}} = 5.3$, while the other 80% of silanols with

$pK_{INT} = 9.2$. This is in excellent agreement with the results obtained by Allen et al, with silica gel solution by potential titration method [15] .

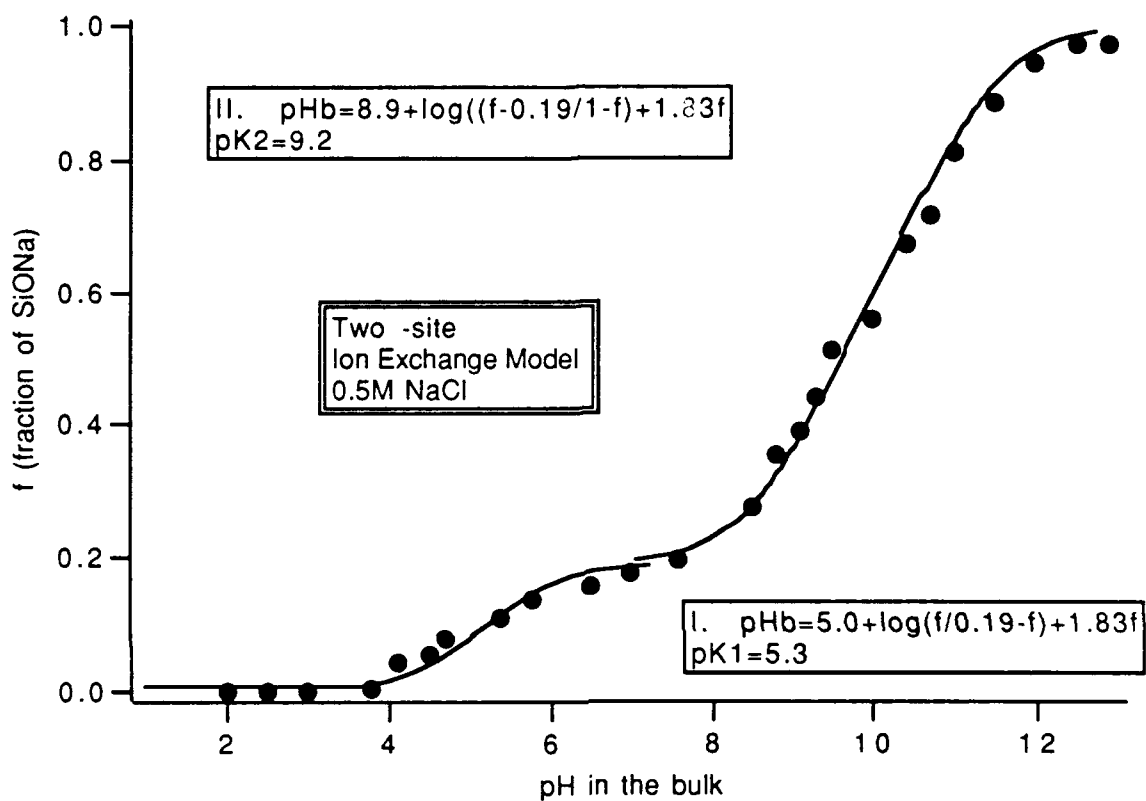


Figure 4.1
 Fraction of SiONa versus bulk pH

4.2 Studies of Molecular Properties at the Surface of a Liquid Jet by Second Harmonic Generation

We report here on the use of surface second harmonic generation to study molecular equilibrium and dynamic processes at the surface of a liquid water jet.[16] The use of a liquid jet is a potentially important way to study interfaces in that it permits the study of equilibrium, e.g., orientational structure and solute adsorption energetics, as well as dynamic molecular processes in systems where the interfering effects of irreversible photochemical and thermal processes can be minimized or avoided by the continuously generated fresh surface. It also offers the possibility of generating desired nonequilibrium populations at an air/liquid interface by controlling the characteristics of the solid/liquid interface of the nozzle immediately prior to the formation of the jet. In this study, it is the dynamics of the adsorption of an organic molecule, p-nitrophenol, to the air/water jet interface that we report.

The initial population density of nitrophenol molecules at the liquid interface that exit the glass nozzle is determined by the nitrophenol interactions at the glass/water interface, not its interactions at the later developing air/water jet interface. Thus, the air/water jet interface has a surface density of nitrophenol molecules that initially is not its equilibrium value. The experiments measure the time it takes the interface to achieve its equilibrium physical and chemical state. From our determination of the jet velocity we know the elapsed time from the jet nozzle to each position along the axis of the jet. The time dependent change in the nitrophenol population at the air/water jet interface can therefore be obtained by measurement of the SH signals at various distances from the jet nozzle. We take the square root of the SH signal, since for a coherent process this is the quantity that is proportional to the number of nitrophenol molecules/cm² at the interface. Using this technique we have been able to study the kinetics and energetics of adsorption of p-nitrophenol to the air/water interface. We found that the adsorption kinetics to the liquid jet/air interface could be described by a dynamic Langmuir model. From the kinetics we obtained the rate constants of $4.4 \pm 0.2 \times 10^4 \text{ sec}^{-1}$ for adsorption and $6 \pm 2 \text{ sec}^{-1}$ for desorption. The free energy of adsorption for the process was found to be $\Delta G_{\text{ads}}^0 = -5.1 \pm 0.2 \text{ Kcal/mole}$, which is the same as for the static (equilibrium) case. The kinetic data also yields the initial surface population of p-nitrophenol at the air/water

interface, which thereby gives information about the adsorption at the preceding glass/water interface of the jet nozzle. We also found that adsorption of p-nitrophenol to the air/water interface is considerably slower than diffusion controlled, thus indicating that the adsorption rate is kinetically controlled by a barrier. The orientation of nitrophenol at the liquid jet /air interface was the same as for the static (equilibrium) liquid/air interface, which indicates that orientational equilibrium was achieved prior to the earliest measurement time, 0.55 msec. In addition, we note that this method offers the possibility of generating various nonequilibrium populations of species at air/liquid interfaces and also opens the possibility of investigating static and dynamic interfacial processes by avoiding the interfering effects of irreversible photochemical and thermal processes common to many systems.

4.3 Phenols and Anilines at the Air/Water interface Surface second harmonic generation has been used to study the adsorption of alkyl phenols and anilines and their respective ions to the air/water interface.[17] The free energies of adsorption of the neutral molecules were obtained using a simple Langmuir model. The quantitative effects of the opposing hydrophobic and solvation forces on molecular adsorption were investigated by varying the chain length of alkylphenolate and alkylanilinium ions. An alkyl chain of at least five carbons was found to be necessary to balance the bulk ionic solvation and thereby bring the ion interface population to a level above the water background. The adsorption of the ions can be quantitatively described by using a modified Langmuir model that includes the electrostatic free energy of the electric double layer as given by the Gouy-Chapmann theory. From the excellent fit of the second harmonic data to this treatment, the chemical and electrostatic free energies of adsorption, interface electric potential, and interface pH were obtained.

5. Ultra-fast Dynamics at the Liquid/Air Interface Studied by Second Harmonic Generation Techniques.

5.1 Photoisomerization Dynamics as a Probe for the Interface The different dielectric (polarity) and transport properties (viscosity) can result in very different static and dynamic properties in the bulk and interfacial regions. To probe the liquid/vapor interface, we used the surface selective technique of second harmonic generation (SHG). We determined how chemical reactions differed in the air/water interface compared with the bulk. We carried out picosecond time resolved measurements of excited state lifetimes of reacting molecules in the air/water interface. In these pump/probe studies we used second harmonic generation methods to probe the dynamics in the interface. We also measured the bulk dynamics of the same process in the same solution using picosecond time resolved fluorescence. In this way we obtained information not only about the interface, by determining how it differs from bulk dynamics, but also about the molecular process itself.

We earlier reported on the photoisomerization of the cyanine dye DODCI in the water/air interface.[18] We measured the SH signal as a function of time delay between the pump and probe pulses. From this study we determined that the photo-induced isomerization time constant is 220 ± 40 ps in the air/water interface versus 520 ± 60 ps for the bulk region of the same solution. The faster rate at the interface could indicate a smaller friction for motion along the isomerization coordinates in the interface.

In addition to these important kinetic results, we also found that the ratio of the yield of trans-photoisomer compared to the cis-isomer was $\phi_{t/c} = 40\text{-}50\%$, which was the same as that found in the bulk aqueous phase. Obviously, the ratio of product yield, i.e., [cis-isomer]/[trans-isomer], does not depend on the barrier crossing dynamics of the excited S_1 to twisted intermediate state, but rather depends directly on the way the twisted polar intermediate decays. The decay of the twisted polar intermediate into either the cis-form or the trans-form depends on the solvent environment. Based on our dynamic measurements it can be argued that the two ground state isomers in the interfacial region experience a similar solvation environment, not unlike that as found in the bulk aqueous phase.

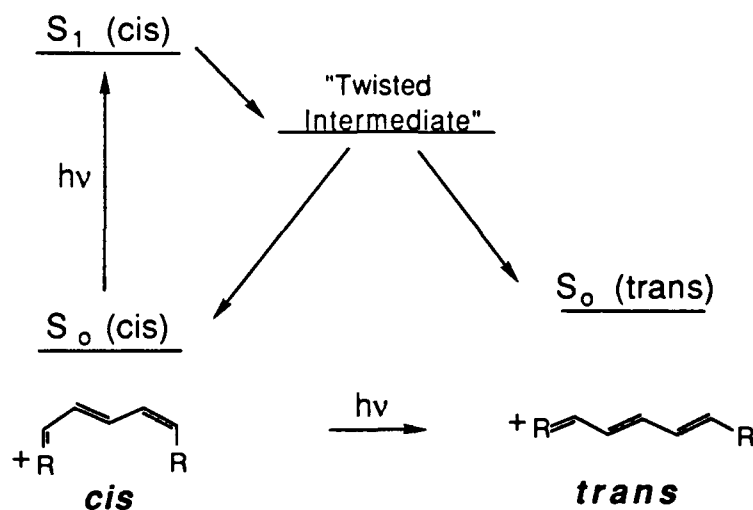


Figure 5.1

Photoisomerization of DODCI (3,3'-diethyloxadicyaniline iodide)

To further explore the influence of the chemical composition of the air-liquid interface on photoisomerization reactions we now have extended our studies of the cyanine dye DODCI at the air/water interface to include the effect of nonpolar molecules at the interface. By varying the chemical composition of the air/liquid interface a corresponding change in the photophysics of the adsorbed cyanine dye molecule was seen. Specifically, we measured the photoisomerization of DODCI at the surface of a spread monolayer of hexadecyl alcohol. The lipid surface provides DODCI with a nonpolar environment. It was found that the surface adsorbed DODCI molecule undergoes rapid isomerization (≈ 300 ps) and $\phi_{t/c} < 10\%$. The fast kinetics for the air-lipid interface is similar to that found for the air-water interface, but is faster than the ≈ 1 nsec time expected for a nonpolar bulk liquid phase. The similar air-liquid photoisomerization kinetics supports, however, our earlier suggestion that the interfacial friction is inherently low compared to what is found in the bulk liquid phase. Finally, the dramatic reduction in $\phi_{t/c}$ for the lipid rich interface (relative to the water surface) is consistent with the solvation properties of the lipid for the DODCI molecule. It is known that $\phi_{t/c}$ in long chain alcoholic solvents is exceedingly low ($< 10\%$), just as what we determined for the air-lipid interface.

5.2 Dynamics of Proton Transfer at the Interface We also investigated the dynamics of proton transfer reactions at the air/water and lipid/water interface. At present there is little direct information on this fundamental reaction in the interfacial region. We made direct kinetic measurements using the pump-probe SHG method already outlined. Specifically, we examined the fast proton transfer reaction of aromatic phenols (such as b-naphthol and p-nitrophenol) as well as aromatic amino compounds (aminopyrene). From bulk work we know that in the excited state these molecules are more acidic ($pK_a^* < pK_a$). By photoexciting the compounds at the interface, we induced an acid-base reaction, which was detected by the time-dependent change in the SH signal.

From the recovery kinetics following photobleaching of aminopyrene at low pH (< 2) we conclude that interfacial deprotonation to form the neutral molecule is rapid (< 320 ps)

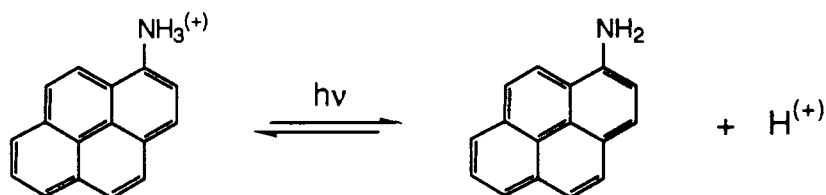


Figure 5.2
proton transfer in aminopyrene

ps). The deprotonation kinetics in the air/water interfacial region are similar to what is known in the bulk aqueous phase. Another example of a proton transfer reaction involves the deprotonation of a neutral molecule to form the charged anion, as exemplified by p-nitrophenol. Again we found that deprotonation time is extremely rapid, taking place in less than 50 ps. This result is important, since we earlier established that under equilibrium

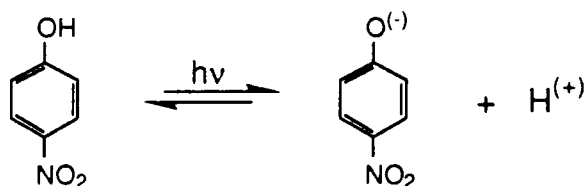


Figure 5.3

Proton transfer in PNP

conditions the anion is repelled from the surface, i.e., it does not adsorb to the surface but remains in the bulk water. The fact that excited state deprotonation (to produce the charged species) does in fact occur at the surface sheds important light on the interfacial solvation of the solute molecule. Presumably the phenolic chromophore is directed sufficiently toward the bulk water molecules so that they can readily accept the proton from the photoexcited phenol, and thereby achieve charge separation.

5.3 Rotational Motion at the Air/Water Interface From SHG experiments, we measured specific elements of the surface nonlinear susceptibility, χ_{ijk} . Figure 5.4 shows the time dependence of χ_{zxx} and χ_{xzx} . At negative time ($t < 0$), before the pump pulse has arrived, we are probing the ground state molecules. Due to photoexcitation, molecules change their nonlinear polarizability, thus the SH signal changes. In the present case, we detected a signal decrease for both elements, which we usually call bleaching. After the initial decrease in signal due to photoexcitation, χ_{zxx} increases and at sometime t it goes even beyond the value corresponding to negative time. Then the signal decays back to the initial value. However for χ_{xzx} , after the initial decrease due to photoexcitation, there is a further decrease in its signal, which later also decays back to the initial value. As it can be seen, our data clearly show a polarization dependence of the dynamics. Different elements of the SH signal show a different time dependence for the relaxation process. This indicates that rotational motions have taken place.[19] If there were no rotational motions involved, the time dependent SH signal for χ_{zxx} and χ_{xzx} would only come from the population term, so the dynamics curve should be the same for both elements, just a population relaxation. However this is clearly not

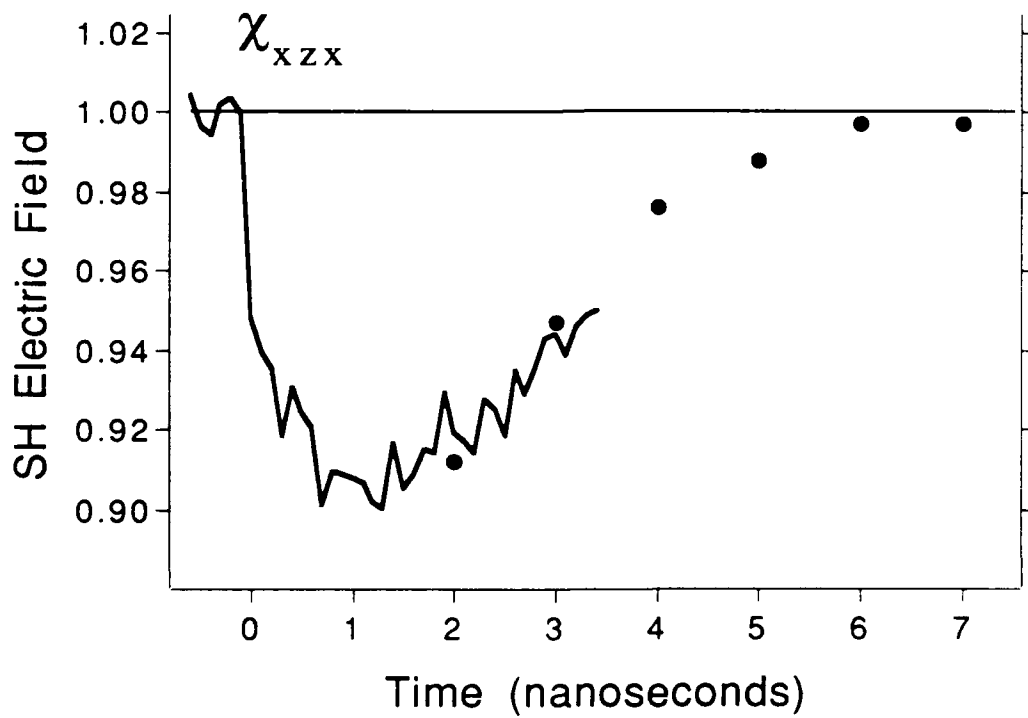
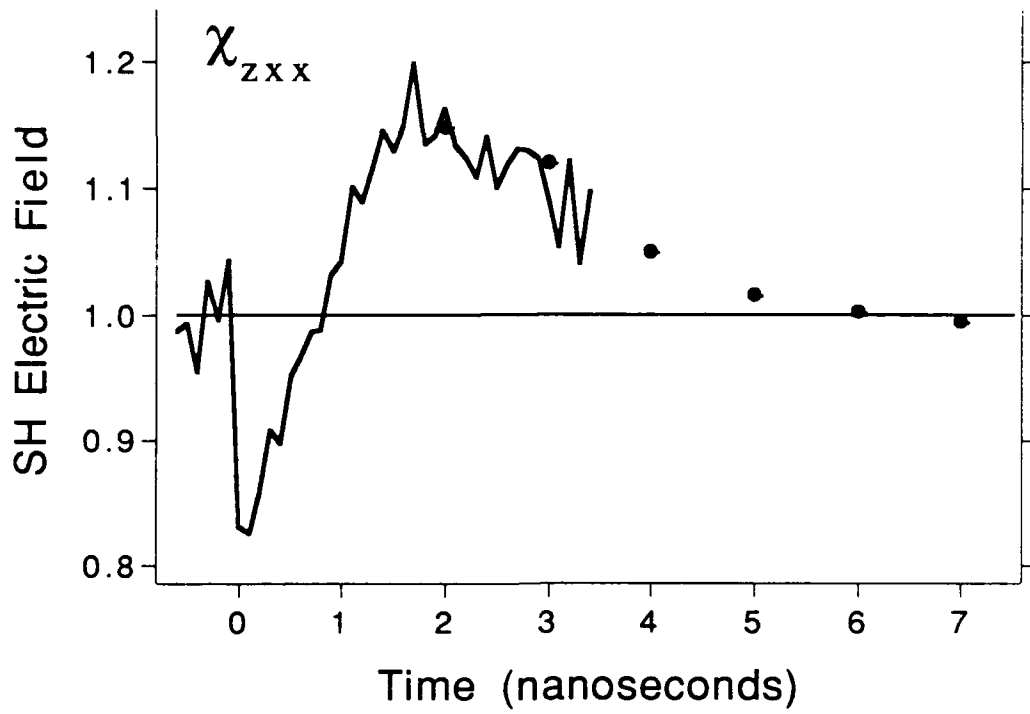


Figure 5.4

the case. Since the SH signal is polarization dependent, we believe that we are observing rotational motions at the air/water interface.

Now, how can we explain the initial decrease in signal due to photoexcitation that we have seen in both elements? At negative time, before the pump pulse has arrived, we are probing ground state molecules, $\chi_{ijk}(t < 0)$. Right after the excitation, but before any population or orientational relaxation has taken place, SH signal can be expressed as: $\chi_{ijk}(t=0)$,

$$\begin{aligned}\chi_{ijk}(t < 0) &= N_0 \langle \alpha^{(2)} \rangle \\ \chi_{ijk}(t = 0) &= N_0 \langle \alpha^{(2)} \rangle - N_s^* (\langle \alpha^{(2)} \rangle - \langle \alpha^{*(2)} \rangle) \\ &\quad \text{(eq 5.1)}\end{aligned}$$

From our experimental data, the SH signal decreased due to photoexcitation. This implies that the nonlinear polarizability of the excited state molecules is smaller than that of the ground state molecules.

There is another interesting feature in our data: at sometime t , the SH signal for χ_{zxx} goes even beyond the initial value at negative time. The difference in signal for χ_{zxx} at time t and at negative time can be expressed as:

$$\Delta\chi_{zxx} = N_s^*(t) (\langle \Omega(t) \rangle^* \alpha^{*(2)} - \langle \Omega(t) \rangle \alpha^{(2)}) \quad \text{(eq 5.2)}$$

where $\langle \Omega(t) \rangle$ is the orientational factor which is related to the direction cosines in terms of the orientational angles. Our data show that $\Delta\chi_{zxx} > 0$ at time t , and we know that the nonlinear polarizability of the excited state is smaller than that of the ground state. Thus the orientational factor for the excited state molecules has to be larger than that for the ground state molecules. This implies that the ground and excited states molecules have different final orientational distributions. A similar argument can be applied to explain the further decrease in χ_{xzx} after the bleaching. Actually, if we substitute the direction cosines for a set of Euler angles, the orientational factor indeed increases for χ_{zxx} and decreases for χ_{xzx} .

In summary, the features of our data are: there are two parts in the kinetic curves. A polarization dependent part at early times, where the SH signal increased in χ_{zxx} but decreased in χ_{xzx} . We think this part is due to the rotational motions at the surface. As it can be seen, this takes place between

500 to 1000 picoseconds. A slow decay which is similar in both elements is probably due to the excitation relaxation of Rh6G molecules at the surface. It is in the time scale of ~ 4 ns which is comparable to the lifetime of Rh6G in the bulk [20].

6. Femtosecond Laser Studies of Electrons in Liquids

6.1 Introduction The properties of electrons in liquids, ranging from hydrocarbons to water, are of widespread interest and are recognized to be important in a wide variety of physical problems such as electrons in amorphous solids, liquid state chemistry, and biological problems such as electron transfer. We have been using femtosecond UV laser pulses to directly study the dynamics of geminate recombination of electrons and cations and the solvation dynamics in neat water. The electrons were generated by multiphoton ionization of neat alkanes and neat water as well as by multiphoton photodetachment of electrons from halide ions and the hydroxide ion in aqueous solutions.

6.2 Electron Solvation Dynamics in Neat Water There are two contrasting descriptions of electron solvation dynamics that have been proposed, the dielectric continuum model (DCM) and the two-state model. The dielectric continuum model (DCM), has been used extensively in simple analytic theories of various chemical processes in polar liquids. [21] It predicts that a continuous absorption spectra blue shift corresponding to the solvent molecular rotation. The two state model means that a wet electron, identifiable by its characteristic absorption spectra, undergoes a transition to the solvated electron. In other words, there are only two electron species present in the kinetics rather than a series of wet electron species, having their own spectra, that evolve into the equilibrium solvated electron. In the two state model, if the absorption of the two species (states) overlap then there must be a wavelength where the two spectra intersect and therefore have the same absorption coefficient ϵ . A consequence of the presence of an isosbestic point can be seen by considering the absorption $A(t)$ at a time t and a wavelength λ .

$$A(\lambda, t) = \epsilon_{\text{wet}}(\lambda) N_{\text{wet}}(t) + \epsilon_{\text{sol}}(\lambda) N_{\text{sol}}(t) \quad (\text{eq. 6.1})$$

where $N_{\text{wet}}(t)$ and $N_{\text{sol}}(t)$ are the concentrations of wet and solvated electrons. At the isosbestic wavelength, $\epsilon_{\text{wet}} = \epsilon_{\text{sol}}$ and the kinetics will therefore be constant after the wet electron is generated since the total electron concentration, $N_{\text{wet}}(t) + N_{\text{sol}}(t)$, is conserved.

To find the isosbestic point we scanned from the near infrared to the visible. The time evolution of the aqueous electron at several different probe wavelengths is shown in Figure 6.1, see next page. For absorption signal at 625 nm, the monotonically rising component corresponds to the appearance of the wet or pre-solvated electron and its transition into the fully solvated electron. At 1000 nm, the absorption increases quickly then decays more slowly. We attribute this decay to the transition from the wet electron to the solvated electron. At 820 nm, there is a rise in the absorption, corresponding to the wet electron formation, then a distinct leveling off of the kinetics. We observed the isosbestic wavelength kinetic behaviour at 820 nm, thus we concluded that the wet to solvated electron transition involves only two states.

Accordingly, we used a simple kinetic model to fit the data.



The quasi-free electron absorption is neglected due to its extended plane waves characterization. Using the known values for the solvated electron absorption [22], the wet electron absorption spectra is obtained, Figure 6.2, which is remarkably similar to the solvated electron absorption spectrum in shape, and a red shift in energy.

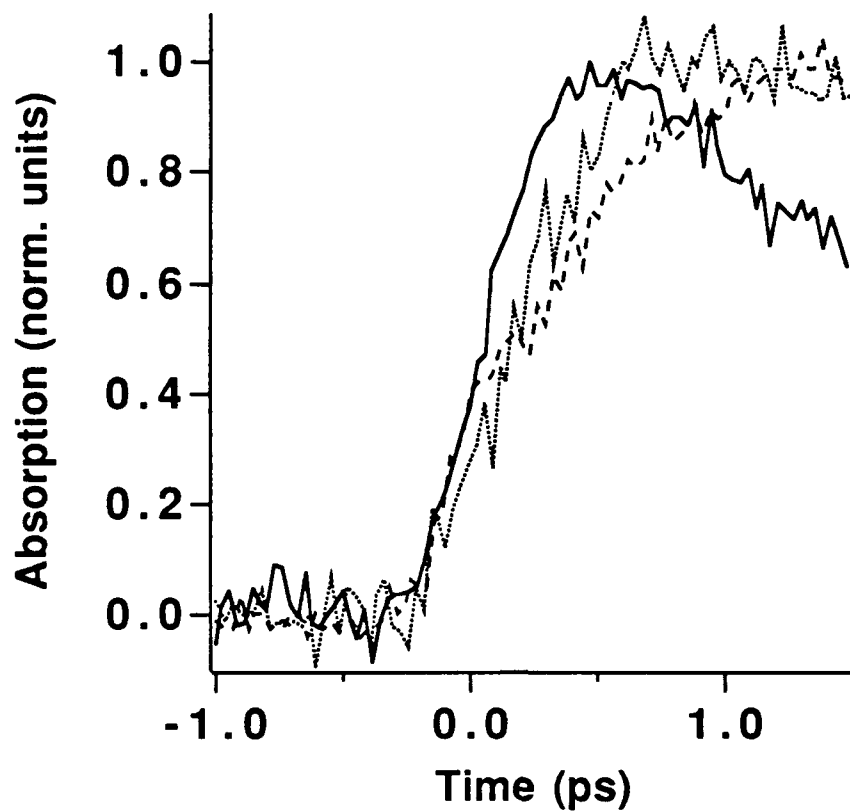


Figure 6.1

Electron Solvation Dynamics In Neat Water

625 nm (broken line), 1000 nm (solid line) and 820 nm (dashed line)

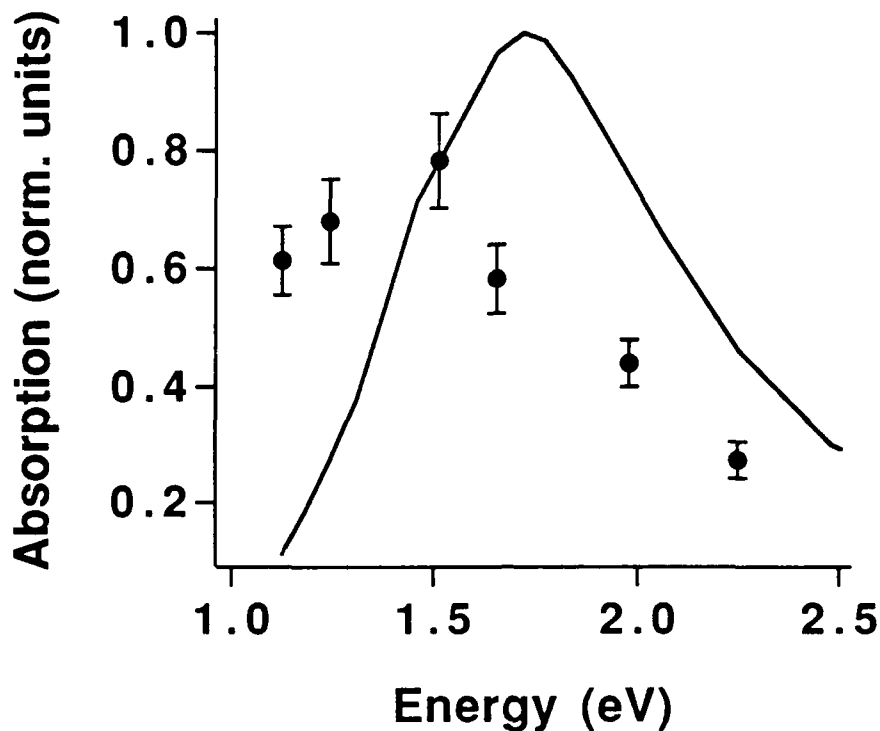


Figure 6.2
Wet Electron Absorption Spectra
wet electron (dots) and the solvated electron (line)

Based on isosbestic wavelength and wet electron absorption spectrum, we hypothesized that the wet electron is just the lowest excited state of the solvated electron. Our experimental results show that the wet electron formation time, $1/k_1$, is 300 ± 30 fs. The lifetime of the wet electron, $1/k_2$, was found to be 540 ± 30 fs. We therefore see that the rate-limiting step in the solvation dynamics of the electron can be really an energy relaxation process like as a radiationless transition in molecules. One anticipates that the internal conversion process can be described by the terms neglected in the Born-Oppenheimer approximation, as is the case with molecules. For the solvated electron, it is reasonable to say that the relevant motions might be water librations. Recent calculations of Rossky, Freisner and coworkers provide theoretical support for the excited state picture. [23]

The role of radiationless transitions in the solvation dynamics of an electron suggests that the solvated electron can be viewed as a kind of molecule which

undergoes a rapid internal conversion to the ground state. In the traditional picture of molecular internal conversion, Frank-Condon factors are the dominant terms in the golden rule expression for the non-radiative rate.[24] To begin to address this question, we have examined the effects of isotope substitution on the solvation dynamics of the electron.

The solvated electron spectra in H₂O and D₂O are the same within a few percent, thus it is quite reasonable to assume that the wet electron absorption spectra are also nearly identical.[22] Therefore differences in the observed solvation dynamics can be directly attributed to kinetic effects. The wet electron formation and decay can be separated by observing the dynamics at the isosbestic wavelength. The dynamics at 820 nm are different for H₂O and D₂O, $1/K_1$ are 300 ± 30 fs and 360 ± 30 fs respectively. At 1100 nm and 625 nm, clear differences are observed also. From fitting the data to equation, values of $1/K_2$, the solvated electron formation time, were found to be 540 ± 30 fs and 600 ± 30 fs. These results are consistent with the overall increase in the average solvation time reported earlier. The large increase in the solvation time upon isotope substitution suggests that librational motions are involved in the rate-limiting step in the solvation dynamics.

6.3 Geminate Recombination of Solvated Electrons In H₂O and D₂O, large non-exponential decays are seen in the absorption signal on the picosecond time scale. All wavelengths studied show the same kinetic behavior.[25] Since there is no wavelength dependence to the data, it suggests strongly that a single species or absorber density decay process is being observed. In addition it is generally believed that the water cation is very unstable in liquid water and within a few tens of femtoseconds reacts with a neutral water to form H₃O⁺ and OH.[26] Thus we are actually observing the recombination of the solvated electron with the hydronium cation.

Comparing the geminate recombination kinetics of H₂O and D₂O, a clear isotope effect is observed. We find that the recombination is slower and more electrons appear to escape recombination in D₂O. To carefully verify the existence of an isotope dependence on the electron thermalization distance, we have compared our data to the Onsager model of electron-cation recombination. [27] Results of the fitting are shown in Figure 6.3. Using an exponential distribution of solvated electrons, the thermalization lengths of 12.4 ± 0.3 Å in D₂O and 11.5 ± 0.5 Å in H₂O are obtained. This indicates that the isotope effect results in larger electron thermalization length in

D₂O than that in H₂O. The physical basis of this result, we believe, is the less efficient energy transfer from the hot photoionized excess electron to the solvent modes in D₂O compared to H₂O.[28] The reduced frequencies mean that more collisions are needed to thermalize the hot electron in D₂O compared to H₂O, thus results larger thermalization distance.

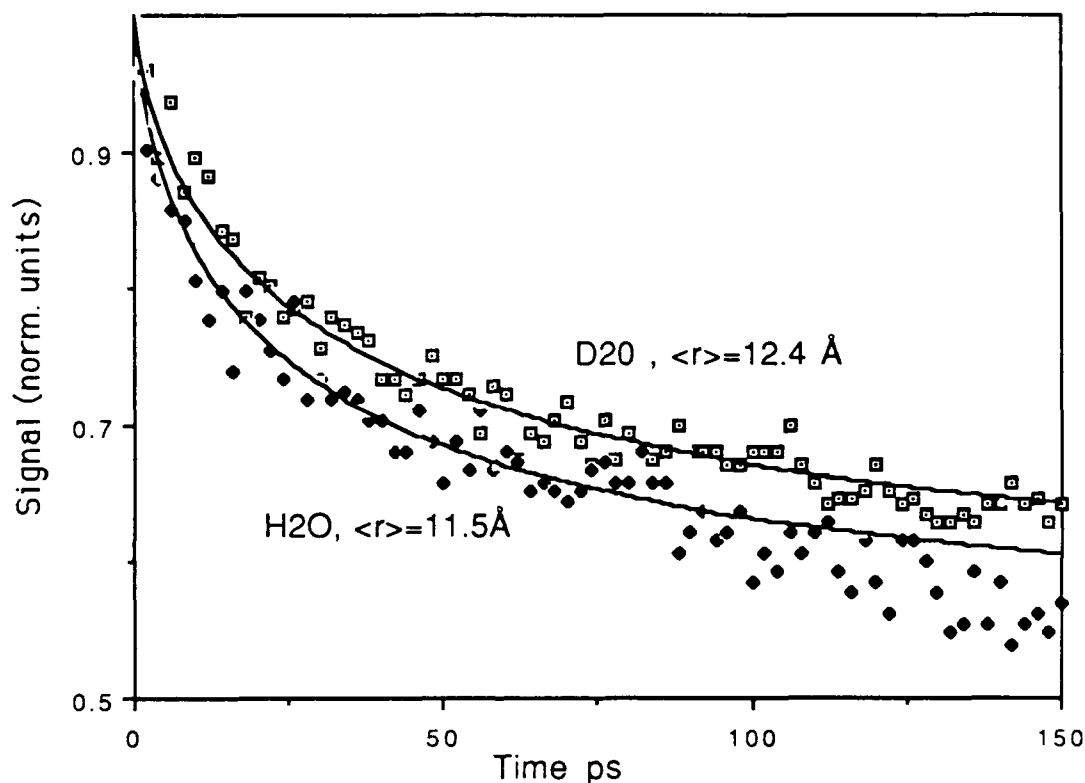


Figure 6.3
Geminate Recombination of Electrons in Water

The electron-cation geminate recombination dynamics studies were also performed in neat alkane solvents. After photoexcitation there can be at least three species in the neat alkane, the electron, the alkane cation and the excited state of the alkane. The electron in an alkane absorbs in the infrared, with a peak around 2000 nm. [$\epsilon=7000 \text{ M}^{-1}\text{-cm}^{-1}$ at 2000 nm for n-hexane] There is, however, a large

absorption tail for the electron that extends well into the near IR and even into the visible at room temperature.[29]

The absorption data for iso-octane is nearly wavelength independent. This suggests that only one single absorber or two species with the same kinetics are being observed. In the IR it is quite reasonable to assume that the electron will be the dominant absorber. CCl₄ quenching experiments showed that there is no absorption of alkane cation at near IR. Linear alkanes were observed excited absorption constant backgrounds, which can be subtracted, at picosecond time scales.

Qualitatively there is a clear correlation between the shape of the molecule, the electron mobility and the observed geminate recombination kinetics. Spherical or branched alkane molecules have comparatively large electron mobilities and fast geminate recombination kinetics. Linear alkanes have much smaller electron mobilities and exhibit slow geminate recombination kinetics. For example the geminate recombination in iso-octane is completed in approximately 0.5 ps, while the geminate recombination in n-octane is significant out to 50 to 100 ps. Using the Onsager model, fits were done by varying mean thermalization distance $\langle r \rangle$ of exponential electron distribution and using the experimentally known values of electron mobility. The above analysis yielded a mean electron thermalization distance of 54 ± 11 Å in iso-octane and 48 ± 10 Å in normal octane.

To further examine the kinetics of geminate recombination, the temperature of the iso-octane was varied. These measurements are qualitatively consistent with the diffusion picture, at higher temperatures the recombination is faster. The comparison to the Onsager model is quite good and the thermalization distances are obtained to be temperature independent. This indicate that the high frequency modes of solvent media are mainly contributed to the kinetic energy dissipation of excess electrons.

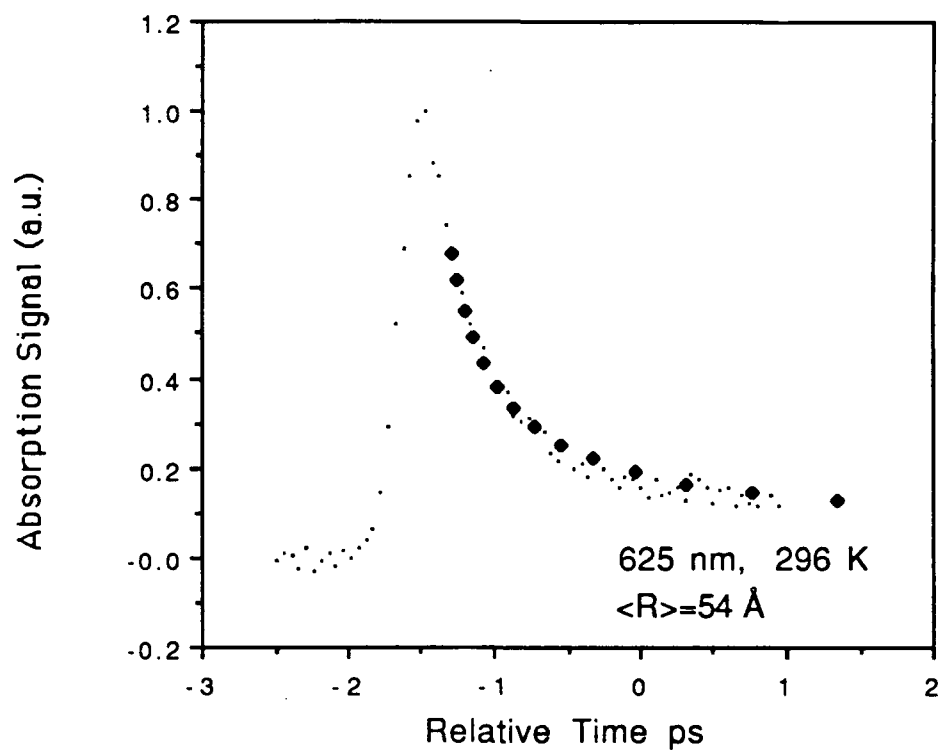


Figure 6.4
Geminate Recombination In Iso-octane

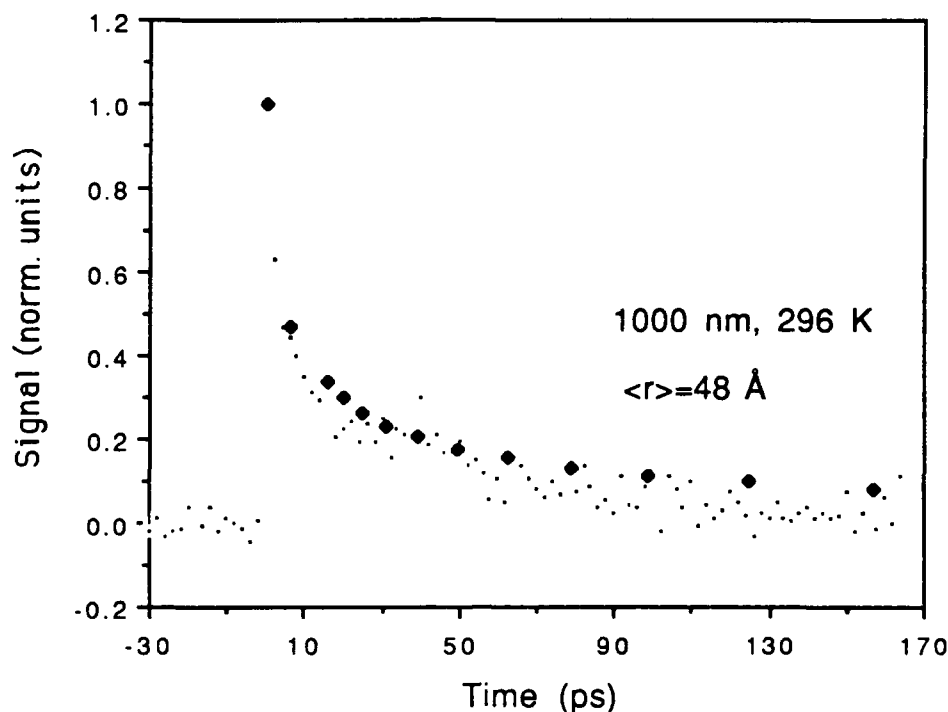


Figure 6.5
Geminate Recombination In n-octane

6.4 Photodetachment of Simple Aqueous Anions Many simple anions in solution, such as halides, have large and broad absorption spectra in the UV. The absorption bands that correspond to the removal of the electron from the ion are called charge transfer to solvent spectra or CTTS spectra.[30] The excited electron will only experience a potential field well due to the orientational polarization of the water molecules, which cannot change on the time scale of optical excitation.

The photodetachment dynamics probed at 625 nm dramatically shows the appearance and rapid disappearance of a new species in addition to the wet and solvated electron.[31] The kinetic behavior indicates that the species is either the electron or $(I^-)^*$, a CTTS excited state. The iodine atom is discounted because it does not absorb in the visible. It is well established that the excited state of the the iodide anion produced upon excitation corresponds to the CTTS state, where the electron is

trapped in the well due to the polarization of the water molecules around the original anion.

Scanning through the visible and near IR wavelength range in 1M iodide aqueous solution, we located an isosbestic point to be at 850 nm. This is very close to the 820 nm obtained for the neat water. From a single exponential fit, the appearance time of the wet electron was found to be 500 fs. This is about 50 % longer than the time found for neat water. However most importantly, the determination of the isosbestic point shows that the wet electron to solvated electron transition is a two-state process in nature. In difference from the neat water case, the wet electron precursor can be observed by visible absorption directly; the trapped electron, i.e. the electron in the very short lived CTTS state.

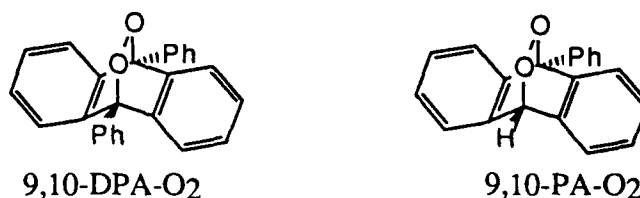


k_1 is the formation rate of the wet electron; k_2 is the formation rate of the solvated electron. The data at all wavelengths were fitted to this model. We obtained the wet electron absorption spectra in the iodide solution, by comparison with the known solvated electron absorption. It is quite similar to the wet electron photoionized from a neutral water molecule. The decay time of the wet electron, $1/k_2$, extracted from the fit was the same as neat water 540 fs. This result and the similarity of the wet electron absorption spectra to that obtained for neat water suggest that the largest deviations from the neat water case occur at early times. Clearly the situation is complex and more investigation is in progress.

7. Picosecond Dynamics of Chemical Intermediates.

7.1 Mechanism of Singlet Oxygen Production from the Photodissociation of Anthracene Endoperoxides The observation of electronic state-selective chemistry provides valuable insight into the nature of chemical reactions. Aromatic endoperoxides are compounds known to undergo wavelength dependent photochemistry. It is well known, for example, that

exciting into S_1 gives products derived from O-O rupture, but excitation to higher states gives 1O_2 and the anthracene moiety. We extended our studies of these molecules, characterized by an O-O peroxide bridge, to better understand the nature of the photofragmentation process and its dependence on the wavelength of the exciting light. We examined two anthracene endoperoxides (9,10-DPA-O₂ and 9,10-PA-O₂).



and

Figure 7.1

The mechanism for the state-selective singlet oxygen producing photochemistry of the anthracene endoperoxides was determined using picosecond laser induced fluorescence methods. For 9,10-DPA-O₂ the ground state aromatic appears in 95 ± 10 ps, whereas for 9,10-PA-O₂ it appears in 60 ± 7 ps. We thus found that the reaction proceeds efficiently from an upper excited singlet state and that it involves a relatively long lived (50 - 100 ps) intermediate, which was describable as having significant biradical character. These results are consistent with our original interpretation given to the photochemistry of two other anthracene endoperoxides (9,10-DMDPA-O₂ and 1,4-DMDPA-O₂).

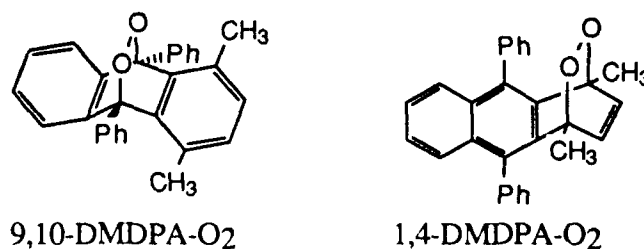


Figure 7.2

Before our work it was widely assumed that photodissociation of endoperoxides was concerted, i.e., it involved the simultaneous rupture of both C-O bonds

leading directly to $^1\text{O}_2$ and the ground state aromatic moiety. Consistent with the observed kinetics as well as the structural dependence on the rates is the following mechanism for $^1\text{O}_2$ production given by Scheme 1.

In summary, the observation of the delayed appearance of the anthracene following photoexcitation into the upper π,π^* S_n ($n, \geq 2$) states as well as structural effects on the kinetics can be explained by an intermediate that is formed either by non-concerted, sequential C-O bond rupture, which involves a 1,6-biradical intermediate, or by the formation of an excited state anthracene valence isomer that has substantial biradical character.

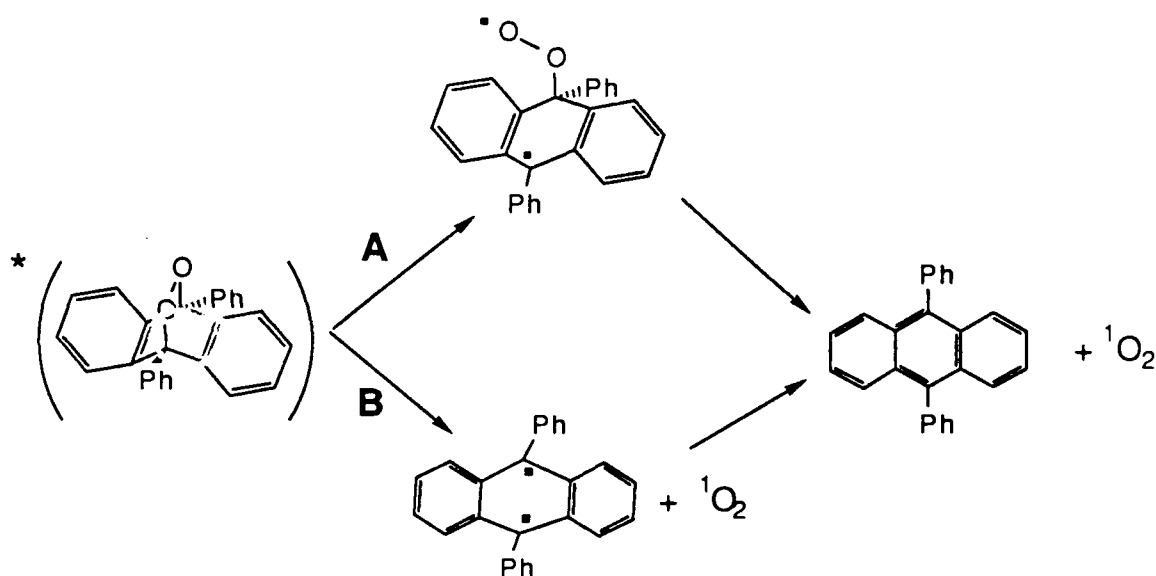


Figure 7.3

Biradical mechanism for upper excited state π,π^* state photofragmentation of aromatic endoperoxides.

7.2 The Chemical Intermediate Dimesityl-carbene - Energetics and Intersystem Crossing Dynamics

It is well known that derivatives of diphenylcarbene exhibit significantly different reaction profiles toward various spin state selective substrates (such as alcohols and olefins). Based on our work and of others, we now know that a key

reason for the variation in reaction efficiencies for the different carbene derivatives is related to corresponding differences in the energy gap (ΔE_{ST}) between the lowest singlet and ground triplet state of the carbenes. Changes in ΔE_{ST} mean that singlet/triplet population ratios change and thus will affect the yields of reaction involving state selective quenchers. From our earlier work we also showed that solvent polarity dramatically alters ΔE_{ST} for a given carbene (ΔE_{ST} decreases with increasing solvent polarity), which affects not only the population of singlet and triplet states but also the intersystem crossing dynamics between the two states.

A particularly atypical diphenylcarbene derivative is dimesitylcarbene (DMC). For instance the chemistry of DMC appears to occur almost exclusively from the ground triplet

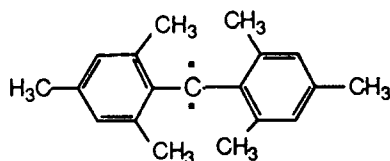


Figure 7.4
Dimesitylcarbene (DMC)

state, unlike that for other diphenylcarbenes. This could be due to an unusually large ΔE_{ST} for DMC, which would make the singlet state inaccessible during the carbene lifetime. A key issue therefore is to establish the energetics and spin relaxation dynamics for DMC and to relate it to the other carbenes.

Using picosecond laser methods we succeeded in determining the spin-relaxation dynamics as well as to establish a lower limit on ΔE_{ST} for DMC. From our results we were able to answer the long standing question about the intersystem crossing dynamics of dimesitylcarbene (DMC) and how it is related to other homologous carbenes. From the solvent polarity dependence we deduced that intersystem crossing in DMC proceeds in the large gap limit, in which the rate of singlet-to-triplet conversion increases as the energy gap decreases. This result is consistent with the large ΔE_{ST} (> 7.5 kcal/mole) that we found for this carbene. The large energy gap was explained by the large bond angle about the central methylene carbon atom, which is caused by steric effects involving the two mesityl groups. This work provides important new

information about the nature of the singlet-triplet splitting and its relation to the dynamics associated with intersystem crossing between the lowest singlet and triplet states of aromatic carbenes.

7.3 Photochemistry in Restricted Environments We investigated how specific local or heterogeneous microenvironments due to molecular encapsulation significantly modify photoisomerization reaction rates. In the case of *t*-stilbene complexed to various cyclodextrins we directly observed how frictional effects due to the local (or "restricted") environment of the inner cyclodextrin cavity modified the motion necessary for reaction, which thereby altered reaction rates. The effects caused by these micro-heterogeneous environments could be rationalized by a simple "lock and key" hypothesis, which is widely used to explain the nature of the guest-host interactions in enzymatic systems.

The *trans-cis* photoisomerization of stilbene is known to occur by a thermally activated twisting around the central double bond,

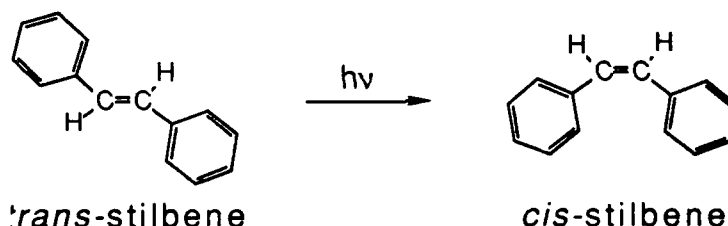


Figure 7.5
Photoisomerization of stilbene

which thus provides the principal mode of deactivation of the excited singlet state of stilbene. From picosecond time resolved methods we have been able to show for the first time that the nature of the complex is different for different cyclodextrins, being dependent mainly on the cavity size of the host molecule (5.6 Å for α -cyclodextrin and up to 8 Å for γ -cyclodextrin). This space limitation affected the chemistry of a reactive guest molecule because it restricted motions that were necessary for the ultrafast photo-reaction and thus altered the rates of reaction. A single complex, with simple reaction kinetics, was found for the stilbene/ α -cyclodextrin complex. This is to be contrasted with the larger

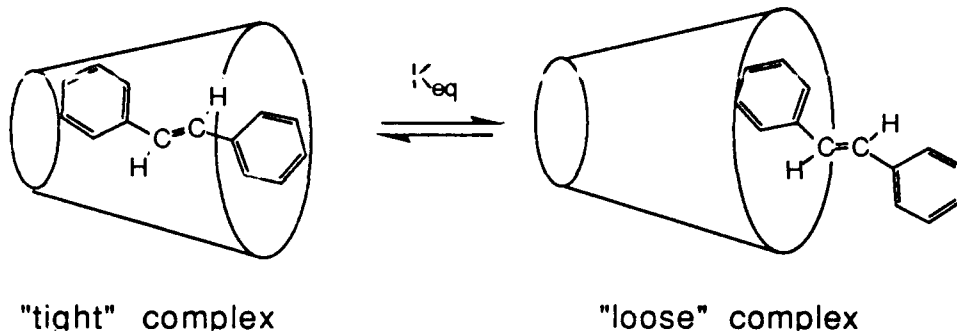


Figure 7.6

Schematic representation of the dynamic equilibrium between "tight" and "loose" stilbene/cyclodextrin complexes

sized cyclodextrins, which yielded two types of 1:1 complexes with the stilbene molecule (e.g. weakly and tightly bound forms). The two distinctly different complexes formed for the larger b- and g-cyclodextrins, yielded vastly different kinetics for the photoisomerization process. For the "tight" complex the guest stilbene molecule is immobilized, yielding slow kinetics (being comparable to the kinetics observed for the molecule in the solid state). In contrast, the "loose" complex undergoes rapid photoisomerization, and is explained by the fact that the local friction (viscosity) experienced by the stilbene molecule is low.

References

1. C. H. Lee, R. K. Chang and N. Bloembergen, Phys. Rev. Lett. 18,167 (1967); N. Bloembergen and P. S. Pershan, Phys. Rev. 128, 606 (1962).
2. N. Bloembergen, Nonlinear Optics (W. A. Benjamin, Inc., Reading, MA)
3. Y. R. Shen, The Principles of Nonlinear Optics (John Wiley, New York, 1984).
4. M. C. Goh, K. B. Eisenthal, Chem. Phys. Lett. 157, 101 (1989).
5. X. Zhao, M. C. Goh, K. B. Eisenthal, J. Phys. Chem. 94, 2222 (1990).
6. S. McLoughlin, Annu. Rev. Biophys. Biophys. Chem.,18,113 (1989).
7. J. T. Davies, Proc. Roy. Soc., A208, 224 (1951).
8. Th. Rasing, H. Hsiung, Y. R. Shen and M. W. Kim, Phys. Rev. A.37, 2732 (1988)
9. N. R. Pallas, B. A. Pethica; J. Chem. Soc., Faraday Trans. I, 83, 585 (1987); M. W. Kim; D. S. Cannell, Phys. Rev. A 13, 411 (1976); M. W. Kim, D. S. Cannell, Phys. Rev. A 14, 1299 (1976).
10. (a) B. Moore; C. M. Knobler; D. Braseta; F. Rondelez; J. Chem. Soc., Faraday Trans. 2, 82, (1986) 1753. (b) M. Losche; H. Mohwald; Rev. Sci. Instrum. 55(12), (1984) 1968 (c) H. M. McConnell; L. K. Tamm, and R. M. Weis; Proc. Natl. Acad. Sci. 31, (1984) 3249. (d) H. Mohwald; Thin Solid Films, 159, (1988) 1
11. P. J. Winch and J. C. Earnshaw, J. Phys. : Condens. Matter 1, 7187 (1989).
12. D. E. Yates, S. Levine and T. W. Healy, J. Chem. Soc. Far. Tran. I, 70 ,1807 (1974).

13. J. A. Davis, R. O. James and J. O. Lockie, *J. Colloid & Inter. Sci.* 63, 480 (1978).
14. G. L. Richmond, *Langmuir* 2, 132 (1986).
15. L. H. Allen, E. Matijevic and L. Meites, *J. Inorg. Nucl. Chem.* 33, 1293 (1971).
16. A. Castro, S. Ong and K. B. Eisenthal, *Chem. Phys. Lett.* 163, 412 (1989).
17. A. Castro, K. Bhattacharyya, K. B. Eisenthal "Energetics of adsorption of neutral and charged molecules at air/water interface by second harmonic generation" to be published JCP.
18. (a) E. V. Sitzmann and K. B. Eisenthal, *J. Chem. Phys.* 90 2831(1989) ;
E. V. Sitzmann and K. B. Eisenthal, *J. Phys. Chem.* 92, 4579 (1988) .
19. T. J. Chuang and K. B. Eisenthal, *J. Chem. Phys.* 57, 5094 (1972);
G. R. Fleming, J. M. Morris and G. W. Robinson, *Chem. Phys.* 17, 91 (1976).
20. R. R. Alfano, S. L. Shapiro and W. Yu, *Opt. Comm.*, 7, 191 (1973).
21. B. Bagchi, D. W. Oxtoby and G. R. Fleming, *Chem. Phys.* 86 (1984) 257;
H. Frohlich, Theory of Dielectrics (Oxford U. Press, New York, 1949)
22. E. J. Hart and J. W. Boag, *J. Am. Chem. Soc.* 84, 4090 (1962).
23. P. J. Rossky and J. Schnitker, *J. Phys. Chem.* 92, 4277 (1988); F. Webster, J. Schnitker, P. J. Rossky, R. Freisner to be published.
24. K. Huang and A. Rhys, *Proc. Roy. Soc. (London)* A204 (1950) 406; R. Kubo and Y. Toyozawa, *Prog. Theo. Thys.* 13 (1950) 160; S. H. Lin and R. Bersohn, *J. Chem. Phys.* 48 (1968) 2732.
25. H. Lu, F. H. Long, R. M. Bowman and K. B. Eisenthal, *J. Phys. Chem.* 93, 27 (1989)
26. F. W. Lampe, F. H. Field and J. L. Franklin, *J. Am. Chem. Soc.* 79,6132 (1957)
27. L. Onsager, *Phys. Rev.*, 54, 554 (1938); K. M. Hong, J. Noolandi, *J. Chem. Phys.* 68 (1978) 5163; 68, 5172 (1978); 68 5026 (1978)

28. F. H. Long, H. Lu and K. B. Eisenthal, Chem. Phys. Lett. 160, 464 (1989).
29. J. H. Baxendale, C. Bell and P. Wardman, Chem. Phys. Lett. 12 347 (1971) ; J. H. Baxendale and E. J. Rasburn, J. Chem. Soc. Faraday Trans., 70 705 (1974)
30. M. J. Blandamer and M. F. Fox, Chem. Rev. 70, 59 (1970) , and references therein.
31. F. H. Long, H. Lu, X. Shi and K. B. Eisenthal, Chem. Phys. Lett. 169,165 (1990)

List of Publications

"Energetics of Adsorption of Neutral and Charged Molecules at the Air/Water Interface by Second Harmonic Generation - Hydrophobic and Solvation Effects"
Castro, A., Bhattacharyya, K. and Eienthal, K.B.
accepted for publication in J. Chem. Phys., 4/91

"Femtosecond studies of electron photodetachment from an iodide in solution:
The
trapped electron"
Long, F. H.; Lu, H.; Shi, X.; Eienthal, K. B.
Chem. Phys. Lett. 169, 165 1990

"Determination of pKa at the air/water interface by second harmonic generation"
Zhao, X.; Subrahmanyam, S.; Eienthal, K. B.
Chem. Phys. Lett., 171, 558 (1990)

"Femtosecond studies of the pre-solvated electron: An excited state of the
solvated electron?"
Long, F. H.; Lu, H.; Eienthal, K. B.
Phys. Rev. Lett. 64, 1469, 1990

"Femtosecond studies of electrons in liquids"
Lu, H.; Long, F. H.; Eienthal, K. B.
J. Opt. Soc. Am. B, 7, 1511 (1990)

"Studies of surface diffusion by second harmonic fluctuation spectroscopy"
Zhao, X.; Goh, M. C.; Subrahmanyam, S.; Eienthal, K. B.
J. Phys. Chem. 94, 3370, 1990

"Effects of long chain molecules on the population and orientation of organic
molecules
at the air/water interface"
Zhao, X.; Goh, M. C.; Eienthal, K. B.
J. Phys. Chem. 94, 222 (1990).

Reply to comments on "Femtosecond studies of electron-cation geminate
recombination in water"
Eienthal, Kenneth B.
J. Phys. Chem., 93, 7534, 1989

"Studies of molecular properties at the surface of a liquid jet by second
harmonic
generation"
Castro, A.; Ong, S.; Eienthal, K. B.
Chem. Phys. Lett., 163(4,5), 412-416, 1989

"Femtosecond studies of electron photodetachment of simple ions in liquid
water:

Solvation and geminate recombination dynamics"

Long, F.H.; Lu, H.; Eisinger, K.B.
J. Chem. Phys., 91(7), 4413-4, 1989

"Effects of solvent polarity and structure on intersystem crossing in diphenylcarbenes:

A picosecond laser study on dimesitylcarbene"
Sitzmann, E. V.; Langan, J. G.; Griller, D.; Eisinger, K.B.
Chem. Phys. Lett., 161(4,5), 353-360, 1989

"Picosecond kinetics of state-selective singlet oxygen producing photochemistry of aromatic endoperoxides"

Sitzmann, E. V.; Langan, J. G.; Hrovat, D. A.; Eisinger, K. B.
Chem. Phys. Lett., 162(1,2), 157-162, 1989

"Femtosecond studies of electron-cation dynamics in neat water: The effects of isotope substitution"

Long, Frederick H.; Lu, Hong; Eisinger, Kenneth B.
Chem. Phys. Lett., 160(4), 464-8, 1989

"The role of translational friction in isomerization reactions"

Bowman, Robert M.; Eisinger, Kenneth B.
Chem. Phys. Lett., 155(1), 99-101, 1989

"Picosecond laser studies on photochemical reactions in restricted environments:

The photoisomerization of *t* - stilbene complexed to cyclodextrins"
Duveneck, G.L.; Sitzmann, E.V.; Eisinger, K.B.; Turro, N.J.
J. Phys. Chem., 93(20), 7166-7170, 1989

"Dynamics of intermolecular electronic energy transfer at an air/liquid interface"

Sitzmann, Eugene V.; Eisinger, Kenneth B.
J. Chem. Phys., 90(5), 2831-2, 1989

"The energetics of orientation at the liquid-vapor interface of water"

Goh, M. Cynthia; Eisinger, Kenneth B.
Chem. Phys. Lett., 157(1,2), 101-104, 1989

Invited Talks 1989-1991

American Chemical Society Symposium on "Energy Transfer and Relaxation," 25-30 August, 1991. Invited Speaker.

EUCMOS XX, 25-30 August 1991, Zagreb, Yugoslavia. Invited Speaker.

International Symposium on Ultrafast Processes in Spectroscopy, October 1991. Bayreuth, Germany. Invited Speaker.

Symposium on "Dynamical Processes in Condensed Molecular Systems, 29-30 April 1991. Neve-Ilan, Israel. Invited Speaker.

International Conference on Coherent and Nonlinear Optics, 24-27 September 1991, Leningrad, USSR. Invited Speaker.

International Workshop on Laser Physics, Dalian Institute of Chemical Physics, 19 May - 1 June 1991. Dalian, China. Invited Speaker.

Center for Analysis of Structures and Interfaces Colloquium "Recent Advances in the Uses of Light in Physics, Chemistry and Medicine, City College, CUNY. 19-21 June, 1991. Invited Speaker.

American Physical Society Symposium on Interfaces, 18-22 March 1991. Cincinnati, Ohio. Invited Speaker.

XV-th International Conference on Photochemistry, 28 July - 2 August 1991, Paris, France. Invited Speaker.

American Chemical Society, Symposium on Classical and Quantal Simulations for Reactive and Solvation Dynamics and Their Critical Experimental Tests, 23-27 April 1990, Boston, Massachusetts. Invited speaker.

Argonne National Laboratory, Symposium on The Solvated Electron-Past, Present and Future, 16-17 July 1990, Argonne, Illinois. Invited speaker.

Gordon Research Conference on the Chemistry and Physics of Water and Aqueous Solutions, 30 July-3 August 1990, Plymouth, New Hampshire. Invited speaker.

Gordon Research Conference on Radiation Chemistry, 9-13 July 1990, Salve Regina, Rhode Island. Invited speaker.

International Centre for Theoretical Physics, Conference on Lasers in Chemistry, 11-15 June 1990, Miramare-Trieste, Italy. Invited speaker.

Naval Research Laboratory, 9 March 1990, Washington, D. C. Invited speaker.

Optical Society of America, Seventh Topical Meeting on Ultrafast Phenomena, 14-17 May 1990, Monterey, California. Invited speaker.

Research Foundation for Opto-science and Technology, International Seminar on Photochemical Dynamics, 25-27 March 1990, Hamamatsu, Japan. Invited speaker.

State University of New York, Buffalo, 21 March 1990. Invited speaker.

University of Michigan, Department of Atmospheric, Oceanic, and Space Sciences, Nineteenth Informal Conference on Photochemistry, 25-29 June 1990, Ann Arbor, Michigan. Invited speaker.

U.S.A.-U.S.S.R. Joint Workshop on Linear and Nonlinear Laser Interactions and Molecular Dynamics, 18-22 June 1990, Moscow, Leningrad, U.S.S.R. Invited speaker.

Rochester American Chemical Society Section's Fall Symposium, University of Rochester, October 8, 1990. Invited Speaker.

NATO Advanced Research Workshop, Tutzing, Bavaria, 10-13 September, 1990. Discussion Leader.

Naval Research Laboratory, Washington, D.C., 9 March 1990. Invited Speaker.

University of Colorado, Boulder, 16 March 1990. Invited Speaker.

State University of New York at Buffalo, 21 March 1990. Invited Speaker.

Union Carbide Corporation, Tarrytown, N.Y., 23 May, 1990. Invited Speaker.

University of Wisconsin, Madison. September, 1990. Invited Speaker.

AT&T Bell Laboratories, Murray Hill, N.J., 23 October, 1990. Invited Speaker.

American Chemical Society, Division of Physical Chemistry, Femtosecond Chemistry Symposium, 10-15 September 1989, St. Louis, Missouri. Invited speaker.

American Chemical Society, Division of Physical Chemistry, Symposium on Chemistry at Solution Interfaces, 9-14 April 1989, Dallas, Texas. Invited speaker.

American Physical Society Meeting, Symposium of the Division of Chemical Physics: Reaction Dynamics in Liquids on Ultrafast Time Scales, 20-24 March 1989, St. Louis, Missouri. Invited speaker.

California Institute of Technology, 18 December 1989. Invited speaker.

Gordon Research Conference on Liquids, 13-18 August 1989, Plymouth, New Hampshire.

Optical Society of America, Quantum Electronics and Laser Science Conference, 24-28 April 1989, Baltimore, Maryland. Invited speaker.

The Pennsylvania State University, 19 September 1989. Invited speaker.

Polytechnic University, 27 September 1989. Invited speaker.

Princeton University, Fourth International Conference on Time-resolved Vibrational Spectroscopy, 11-16 June 1989, Princeton, New Jersey. Invited speaker.

Stanford University, 5 December 1989. Invited speaker.

University of California, Berkeley, 21 November 1989. Invited speaker.

University of California, Irvine, 11 December 1989. Invited speaker.

University of California, San Diego, 14 March 1989. Invited Speaker.

University of Rochester, 4 October 1989. Invited speaker.